3D geometry and architecture of a normal fault zone in poorly lithified sediments: A trench study on a strand of the Baza Fault, central Betic Cordillera, south Spain

Iván Medina-Cascales, Leah Koch, Néstor Cardozo, Iván Martin-Rojas, Pedro Alfaro, Francisco J. García-Tortosa

PII: S0191-8141(18)30483-8

DOI: https://doi.org/10.1016/j.jsg.2019.02.003

Reference: SG 3801

To appear in: *Journal of Structural Geology*

Received Date: 10 October 2018

Revised Date: 8 February 2019

Accepted Date: 11 February 2019

3D geometry and architecture of a normal fault zone in poorly lithified sediments: A trench study on a strand of the Baza Fault, central Betic Cordillera, south Spain

Iván Medina-Cascales[1], Leah Koch[2], Néstor Cardozo[2], Iván Martin-Rojas[1*], Pedro Alfaro[1] and Francisco J. García-Tortosa[3]

[1] *Departamento de Ciencias de la Tierra y del Medio Ambiente, Universidad de Alicante, 03080 Alicante, Spain*

[2] *Department of Energy Resources, University of Stavanger, 4036 Stavanger, Norway*

[3] *Departamento de Geología, Universidad de Jaén, Campus Las Lagunillas, 23071 Jaén, Spain*

Abstract

Successive excavation of 13 trenches of different orientations reveals the complexity of a normal fault zone in Pliocene-Pleistocene unconsolidated sediments on a strand of the Baza Fault, central Betic Cordillera, south Spain. These trenches and the excavation floor are interpreted and integrated to reconstruct the 3D geometry and internal architecture of the fault zone. The structure consists of two main fault strands: an eastern one with a few hundred metres throw and a western one with at least 15 m throw. These strands interact and gradually merge to the south, bounding a main deformation zone narrowing from ~7 to 1 m along strike. Fault-bounded rock bodies, clay and sand smears, and clay injections define the structure. These features are highly variable in 3D. In the northern part of the outcrop, deformation is localized around the main strands, brittle in the west and more ductile to the east. As the strands and their fault zones increasingly interact, fault throw, rock deformation and maturity of the structure increase. Mechanical stratigraphy also controls the style of deformation. A realistic representation of this 4D picture of fault deformation is critical for modelling fluid flow in shallow to possibly deep, faulted sedimentary reservoirs.

Keywords: Normal fault zone, poorly lithified sediments, fault smears, clay injection, trench study.

1. Introduction

Fault zones are narrow, irregular rock volumes characterized by high internal complexity, heterogeneous deformation, and petrophysical properties that differ from those of the host rock (Wibberley et al., 2008; Childs et al., 2009; Faulkner et al., 2010; Bense et al., 2013). The description and interpretation of fault zone geometry, architecture and evolution are important for understanding and predicting the impact of faults on fluid flow in the upper crust, including groundwater flow (Bense and Van Balen, 2004; Bense and Person, 2006; Folch and Mas-Pla, 2008), hydrocarbon migration, entrapment and production (Grauls et al., 2002; Sorkhabi and Tsuji, 2005; Manzocchi et al., 2010; Wibberley et al., 2017), hydrothermal flow and mineralization (Rowland and Sibson, 2004; Person et al., 2008; Fairley 2009), nuclear waste storage (Ofoegbu et al., 2001; Gray et al., 2005), and CO_2 sequestration (Shipton et al., 2004; Agosta et al., 2008; Dockrill and Shipton, 2010). The internal structure of a fault zone may also affect its seismogenic behaviour (Sibson, 1986; Scholz, 2002; Sibson, 2003; Rice and Cocco, 2007).

The basic model of a fault zone includes two main architectural elements, which are the fault core and the damage zone (Caine et al., 1996). The fault core accommodates most of the fault displacement and strain and is composed of fault rocks (Braathen et al., 2009; Gabrielsen et al., 2017), single or multiple slip surfaces (Caine et al., 1996), and/or clay/shale smears (Vrolijk et al., 2016) that may have undergone structural diagenesis (Eichhubl et al., 2005 and 2009; Laubach et al., 2010; Solum et al., 2010). The damage zone is made up of secondary structures such as smaller faults, folds, fractures, and/or deformation bands (Shipton and Cowie, 2001 and 2003; Kim et al., 2004, Fossen et al., 2005). In poorly lithified sediments, mixing of sediments can occur in the fault zone, forming a “mixed zone” located between the fault core and the damage zone (Heynekamp et al., 1999; Rawling and Goodwin, 2006; Loveless et al., 2011; Braathen et al., 2013).

All the aforementioned elements form heterogeneities and anisotropies within the fault zone, whose geometry and internal architecture can vary significantly over short distances along both strike and dip (Childs et al., 1996; Foxford et al., 1998). The challenge of describing fault zones due to their high spatial variability has triggered the need to carry out detailed outcrop studies. There are many studies, but few provide a truly three-dimensional exposure of the fault zone. Exceptions are open-cast mines and unconsolidated sediments, where the fault zone can be excavated and its 3D geometry and internal structure reconstructed (Lehner and Pilaar, 1997; Childs et al., 1997; Kristensen et al., 2008; Kettermann et al., 2016).

The present study contributes to the current efforts on fault zone characterization by describing and interpreting an excellent outcrop dataset pertaining to a normal fault zone in one of the main strands of the Baza Fault (south-central Spain). This strand juxtaposes poorly lithified sediments against each other, which makes this normal fault an extraordinary natural laboratory to study the mechanisms that led to the development of a highly complex internal fault structure. Following a methodology similar to that of Kristensen et al. (2008) but at a larger scale, the fault zone was systematically excavated through a series of 13 trenches, mostly oriented perpendicular to the fault strike, resulting in a total excavation volume of ~15×15×4 m^3. Interpretation and correlation of the 13 sections and of the excavation floor led us to the construction of a 3D model displaying the fault zone architecture. Analysis of the distribution of deformation and deformation styles allowed us to assess the fault zone evolution. These results provide insight for the upscaling, subsurface imaging, and reservoir modelling of highly complex fault zones in poorly lithified sediments.

2. Geological setting

The Baza Fault (BF) is located in the central Betic Cordillera (south-central Spain) within the Guadix-Baza Basin (Fig. 1). It is an active, ~37 km-long normal fault array striking N-S to NW-SE and dipping 45 to 65° E (Alfaro et al., 2008; García-Tortosa et al., 2008; Fernández-Ibáñez et al., 2010; Sanz de Galdeano et al., 2012, Castro et al., 2018). Overall, the BF accommodates ENE-WSW extension in this area (Alfaro et al., 2008, and references therein). The BF consists of a fault array of variable width and number of fault strands, which along strike can be divided into two main sectors. In the northern sector, the BF strikes N-S and extends from its northern termination to Baza (Fig. 1). There, the fault array consists of a narrow, 0.1 to 1 km-wide zone comprising a few sub-parallel fault strands. The southern sector strikes NW-SE and runs from the town of Baza to the southern termination of the BF (Fig. 1). There, the deformation is distributed within an up to 7 km-wide zone composed of several fault strands.

The total throw of the BF is ~2 km (Alfaro et al., 2008). The long-term vertical slip rate ranges between 0.12 and 0.49 mm/yr (Alfaro et al., 2008; García-Tortosa et al., 2011; Sanz de Galdeano et al., 2012). The BF was the seismogenic source of the 1531 Baza earthquake (MMI=VIII-IX), which destroyed the town of Baza (Martínez Solares and Mezcua, 2003, Sanz de Galdeano et al., 2012).

The BF controlled the sedimentary depocenters of the Guadix-Baza Basin during the late Miocene to Pleistocene (García-Tortosa et al., 2008,). In fact, the fault separates the basin into two main depocenters: the Guadix sub-basin to the W, primarily filled with alluvial silts, sands, and conglomerates, and the Baza sub-basin to the E, which is a half-graben primarily filled with lacustrine and palustrine marls, limestones, clays, and gypsum (Vera, 1970; Viseras, 1991; Gibert et al., 2007b; Pla-Pueyo et al., 2011; Haberland et al., 2017) (Fig. 1).

The study area is located in the northern sector of the BF (Fig. 2). Here, the fault array is ~1 km wide and is bounded by the Guillén and Carrizal fault strands (Fig. 2), which juxtapose multiple blocks of different ages (Fig. 2b). The western block lies on the footwall of the Guillén strand and consists of Lower Pliocene (~5 Myr) fluvio-alluvial deposits of the Guadix Formation (Agustí et al., 2001). The central block lies in between the Guillén and Carrizal strands and includes Upper Pliocene-Lower Pleistocene (~2.8 Myr) lacustrine units (units 1 and 2; Peña, 1985). The eastern block is located on the hanging wall of the Carrizal strand and consists of Lower-Middle Pleistocene (~1.2-0.9 Myr) lacustrine deposits (unit 3; Gibert et al. 2007a). 8 secondary fault strands are identified in the study area; however, most of the offset is localized along the Guillén and Carrizal strands. According to both ages of the faulted deposits and estimated fault slip rates, these two faults are characterized by at least a few hundred metres of throw. The trench area is located in the Carrizal strand (Fig. 2a).

3. Methodology

We excavated a series of trenches in the Carrizal strand of the BF (Fig. 3a). A total of 13 vertical trenches were excavated, 10 striking E-W (A00, A0, A1, A2, A3, A4, A5, B0, B1, and B3), and 3 striking N-S (C1, C2, and C3), all of them complemented by the floor sections after excavation.

The E-W trending trenches are approximately 12 m long and 4 m high, whereas the N-S trending trenches are approximately 4 m long and 4 m high. Once a trench face was exposed, it was cleaned using sharp tools to remove debris and disturbed material. The surface was then marked by a 1×1 m grid; then, each square was photographed at high resolution. Lastly, each trench was surveyed with a terrestrial LiDAR scanner from at least 3 different locations to ensure total coverage. LiDAR point clouds contain both x, y, z coordinates and RGB colour information.

The individual photographs were corrected for distortions (e.g., lens distortion and orthocorrection) and then stitched together into photomosaics using the Hugin software. The photomosaics were subsequently georeferenced with the ArcGIS software and draped over the LiDAR point cloud using the LIME software. Such procedure recreated the trenches in 3D with accurate locations and high-resolution (cm) imagery.

The interpretation was first performed in 2D on the high-resolution photomosaics (Fig. 3b) and then redrawn on the 3D LIME model (Fig. 3c). All the lithological boundaries were identified by considering textural differences and colour changes because the compositions of most of the units were not distinguishable. Fault traces were easily identified by the offset and truncation of individual sedimentary beds. Some of the structures, notably in the SE quadrant, were difficult to interpret due to the high level of deformation and mixing of the sedimentary beds. Because of different field campaigns and different coordinate origins, trenches A00 and A0 were not co-referenced with respect to trenches A1 to B3. Accordingly, the 3D model was limited to the area encompassed by sections A1 to B3 (Fig. 3a).

The 3D model was constructed by means of the Move software. Both fault and horizon surfaces were created by interpolating their traces on the trenches using ordinary kriging (Fig. 3d). This method was sometimes unsuccessful in reconstructing the highly deformed and folded horizon surfaces, so more elaborate techniques were utilized. In case of a fold, two or more separate surfaces were created on opposite sides of the fold hinge and then converted to points to reproduce an accurate fold surface geometry. Finally, surfaces were tested for accuracy (i.e., fit to the interpreted horizons and fault traces), continuity, and consistency. Slicing of the 3D model along horizontal sections was used to visualize the variation in the fault zone with depth.

4. Architecture and deformation of the fault strands

In the study area (Fig. 4a), we identify two main normal fault zones, an eastern fault zone corresponding to the Carrizal Fault (EF), and a western one corresponding to the Western Fault (WF). Each one of these fault zones comprises a fault core surrounded by damage zones. Together, they subdivide the area into three different blocks characterized by different stratigraphic units (Fig. 4b-c): a western block corresponding to the WF footwall and composed mainly of Pliocene carbonate silts (unit 1, ~2.8 Myr), an eastern block corresponding to the EF hanging wall and consisting of Middle Pleistocene silts and limestones (unit 3, ~1.2-0.9 Myr), and a middle block lying in the WF hanging wall and EF footwall and formed by interlayered Pliocene carbonate silts, clays, sands and gravels (unit 2, ~2.8 Myr) (Gibert et al., 2007b; Castro et al., 2018).

Because there are no common stratigraphic markers among the blocks, it is not possible to accurately estimate the throws of both the WF and EF. Hence, according to the age of units 1 to 3, we estimate the EF throw on the order of hundred of metres and the WF throw greater than a ten of metres (see section 4.2).

The WF and EF are separate in the northern portion of the study area. However, they gradually merge southwards where the trench area is located. Within the trench area, the amount of deformation is lower in both the western and eastern blocks with respect to the middle block (Fig. 4c), so we use the term main deformation zone (MDZ) to refer to the middle block.

4.1 Stratigraphic framework

Stratigraphic units 1, 2, and 3 were split into 23 informal subunits on the basis of their texture, composition and colour (Fig. 5). Since it is difficult to determine the stratigraphic thickness of these units due to the high amount of deformation they have undergone, we refer merely to their maximum thickness measured in the individual trenches.

Unit 1 includes subunits 1A to 1H (Figs. 4b and 5), which are conformable and are composed of lacustrine, white to light grey and pink, slightly consolidated carbonate silts locally interbedded with mm- to cm-thick dark clay levels. Subunit 1B differs from all the others because it is formed by an ~1 m-thick bed of dark grey to yellow laminated clay. Subunit 1G also shows a high clay content.

Unit 2 comprises subunits 2A to 2N (Figs. 4b and 5), which are also conformable. This unit is characterized by a lacustrine multilayer package of alternating brown, yellow and grey, cm-thick, slightly consolidated carbonate silts and mm- to cm-thick dark grey clay levels. In particular, while subunits 2E, 2H, 2J and 2M show more clay, subunits 2F, 2G and 2L mainly include carbonate silt levels. Subunit 2B stands out as an ~1.2 m-thick body of reddish mm- to cm-thick gravels embedded in a coarse sand matrix (Fig. 5). Thin red sand levels are also present in both underlying and overlying subunits 2A and 2C, respectively. Subunit 2I consists of an ~70 cm-thick, dark grey laminated clay with sparse cm-size gypsum crystals (Fig. 5).

Unit 3 consists of lacustrine, white to yellow laminated silts and sands interbedded with white laminated micritic limestones, which are overlain by m-thick micritic limestone beds (Fig. 5). In the northern part of the trench area, a fluvial terrace unconformably overlies the highly deformed Plio-Pleistocene deposits (Fig. 6a).

4.2. Fault zone architecture

Photomosaics and interpretations of all the excavated sections, both trenches and floor, are included as supplementary material. The interpretations of three E-W trending trenches, A0, A5 and B3, are shown in Fig. 6, whereas interpretation of the floor of the excavation is shown in Fig. 7. Figure 8 includes a stratigraphic chart summarizing the inferred correlations among all the subunits documented within the trenches. Faults and fault-bounded rock bodies (horses, sensu Gibbs 1984 and Childs et al. 1997) are indicated by a letter and a number. Main slip surfaces are represented with red lines. Tables 1 and 2 summarize the descriptions of faults and rock bodies, respectively. Fig. 9 shows depth slices at 1 m intervals through the 3D model of the fault zone. Although these slices are not as detailed as the study sections, the main geologic features are well represented in the slices, and they fit the interpreted sections (e.g., Figs. 7 and 9e), confirming that the 3D model is a fair representation of the 3D variability of the fault zone.

4.2.1. Western block

The western block is divided into several rock bodies (H1 to H5) bounded by normal faults F1 to WF (Figs. 7 to 10 and Table 2). WF strikes ~330° in the N, and it bends towards ~300° southwards (Figs. 7, 9 and 11a). On average, WF dips 60°E, and it is made up of layered gouge, sand layers, carbonate breccia, and thin clay membranes incorporated by a clay smearing process (Fig. 8 and Table 1). This fault infill is bounded by slip surfaces. The minimum amount of throw along WF is equivalent to the thickness of unit 2 in Fig. 5, which is ~15 m.

Normal faults F1 to F3 (Figs. 7 to 10) crosscut the western block. F3 is an E-dipping fault trending approximately parallel to WF (Figs. 7, 9 and 11b) and has a throw exceeding the outcrop height, which is ~4 m (Table 1). West of F3, the western block is offset by minor synthetic normal faults F1 and F2. F2 strikes ~330° and is characterized by variable throw from 0.2 to 1.4 m (Fig. 8 and Table 1). F2 intersects and offsets F1, which strikes ~285°, dips N, and shows variable amounts of throw from 0.3 to 2 m (Figs. 7 to 9 and Table 1).

Continuous and semi-continuous thin clay smears are documented between F1 to F3 slip surfaces (Fig. 8 and Table 1). F1 to F3 divide the western block volume into rock bodies H1 to H5 (Table 2). According to the arrangement and the estimated throws of these faults (Table 1), H1 lies in the highest structural position, and the structures progressively step down into H2, H3, H4, and H5 (Fig. 10).

4.2.2. Main deformation zone (MDZ)

The main deformation zone (MDZ) is bounded by faults WF to EF (Figs. 7 to 10). The EF main slip surface strikes ~330° and dips ~60°E. It contains a semi-continuous to ruptured thin clay smear (Fig. 8 and Table 1), and in contrast to WF, it does not vary significantly in strike, which leads to narrowing of the MDZ southwards (Figs. 7, 9 and 11a).

Faults F10 to F80 internally offset unit 2 (Figs. 7 to 10). These faults can be classified into three main families (Fig. 7 and Table 1): α faults striking ~330° mostly parallel to EF (F10, F20, F21, F60, F70, F79 and F80), β faults striking ~300° approximately parallel to the southern segment of WF (F12, F22, F30, F31 and F40), and γ faults striking ~220° (F50 and F51).

The α faults F10, F60, F70 and F80 stand out due to their larger throws and continuity along the MDZ (Fig. 8). F10 runs along the western part of the MDZ. It displays a throw > 4 m in trench A3 and < 0.5 m in trenches A2 and B0 (Fig. 12). In trench C3, F10 crops out close to F20, and their two slip surfaces join southwards into F30 (Figs. 9a-c, 10 and 11c). F60 and F70 are located in the NE part of the fault zone (Figs. 7 and 9d-e). They have throws > 4 m (Fig. 12), large amounts of clay infill bounded by slip surfaces (Fig. 6a and Table 1), and are intersected by β fault F40 (Fig. 11d). F80 runs along the MDZ with a gentle slip surface dipping ~40° in the central part of the excavation and steepening southwards (Figs. 9 and

11e). F80 has a throw > 4 m (Fig. 12) and contains several thin clay smears (Fig. 8). In trench A5, it consists of two upwardly converging slip surfaces with a large amount of clay from subunit 2I between them (Fig. 6b).

Other significant faults are F20, F40, F50 and F51 (Fig. 9). F20 is an α, sub-vertical to W-dipping fault splaying from F10 (Fig. 11c) and having throws that vary between 0.2 and 2.7 m, with its lowest values in trenches A3 and C3 (Fig. 12). In trench A3, F20 develops an extensional relay that allows the incorporation of clay from unit 2I between two slip surfaces (Fig. 13a) (Lehner and Pilaar; 1997). F40 is a β, sub-vertical fault extending from F10 to EF and separating the northern horses from the central horses (Figs. 9 and 11f). F50 is a γ, sub-vertical fault between F10-F20 and F80 (Figs. 9 and 11f). F50 consists of two slip surfaces, F50a and F50b, merging both upwards and to the W with cm- to m-thick clay infill from subunit 2I between them (Figs. 9 and 11f). This fault acts as an oblique boundary between the central and southern horses. Antithetic faults also occur in the MDZ. The most important is F51, a γ fault conjugate to F10 that tips out towards the clay-rich subunit 2I (Figs. 9d and 13b).

All these faults divide the MDZ into rock bodies H10 to H92. We divide them into five main sets (Fig. 10 and Table 2): the western set (H10, H11, and H12) bounded by faults WF, F10 and F30; the northern set (H20, H21, H30, and H40) limited by F10 to the W, EF to the E, and F40 to the S; the central set (H50, H51, H60, H61, and H70) bounded by F10 to the W, F40 to the N, F80 to the E, and F50 to the S; the southern set (H79, H80, and H81) bounded by F30 to the W, F50 to the N, and F80 to the E; and the eastern set (H90, H91, and H92) limited by F80 to the W and EF to the E (Table 2). According to the arrangement of the faults and their estimated throws (Fig. 12), the structural positions of these sets from top to bottom are first the western set, followed by the northern set, the central set, the southern set, and the eastern set (Fig. 10).

4.2.3. Eastern block

The eastern block on the hanging wall of EF has no prominent internal faulting. The main structure in this block is a syncline in contact with EF (Fig. 6a-c). The wavelength of this fold varies from ~ 1 m in trench A0 (Fig. 6a) to ~ 3 m in trench B3 (Fig. 6c), and the bedding dips vary from ~60º E near EF to ~10° E to the E.

4.3. Deformation

Deformation in the fault zone is heterogeneous. For a better understanding of these heterogeneities, we describe them along three orthogonal directions: X (E-W, orthogonal to the main strands), Y (N-S, parallel to the main strands) and Z (vertical).

Along the X direction and starting from the west, horses H1 to H4 in the western block show minimal internal deformation, with unit 1 gently dipping to the N (Fig. 7). Deformation increases eastward and concentrates around the two main faults WF and EF, which bound the MDZ. In the northern and central trenches (Fig. 6a-b), these faults have well-developed fault zones consisting of a fault core and a surrounding damage zone (sensu Caine et al., 1996). In the case of WF, its fault core is represented by a layered, mm to ~20 cm-wide fault gouge, layered sand, clay and micrite breccia (Table 1), as well as horse H10 in central sections of the MDZ (Fig. 6b). The WF damage zone consists of two narrow bands developed in the footwall (H5 in the western block) and hanging wall (H10 in the MDZ), both dipping towards the downthrown side of the fault. These bands are deformed by minor faults accommodating the rotation and stretching of the beds and are similar in width (~1-2 m), so the damage zone is almost symmetrical. On the other hand, EF has a more complex fault zone. An ~1-2.5 m-wide band of most intense deformation in the MDZ in contact with EF is characterized by high-throw faults (F60 to F80), highly deformed rock bodies (H40 and the eastern set), clay smears, and clay bodies between fault slip surfaces that we interpret as clay injection structures. We consider this band the EF fault core (Fig. 6a-b). The EF damage zone is represented on its footwall (MDZ) by an ~3-4 m-wide zone in unit 2 limited by faults F10 to F51 and on its hanging wall (eastern block) by the ~2 m-wide syncline in unit 3 (Fig. 6). Thus, the EF damage zone is asymmetrical, with most of the deformation accumulated in the footwall.

Along the Y direction, the most remarkable change is the southward narrowing of the MDZ from ~7 m wide in the N (Fig. 6a) to ~1 m wide in the S (Fig. 6c). The distribution of deformation along the X direction in the MDZ also varies with location along the Y direction. In the northern trenches, deformation along the X direction is characterized by western and central less-deformed zones and an eastern highly deformed zone close to EF (Fig. 6a). In the central trenches, deformation increases in the west near WF (Fig. 6b). Central set horses are offset by minor synthetic and antithetic faults, e.g., F51 (Fig. 9d), which accommodate extension and are responsible for related structures such as horsts, grabens and domino faults (Fig. 13c). Clay-rich base (subunit 2I) and top (subunit 2K) boundaries of H61 act as detachment levels, and subunit 2I is stretched into boudins (Fig. 13c). The most significant variation occurs in the southern trenches B0 to B3, where the deformation increases dramatically and bedding can barely be recognized (Fig. 6c). Fault throw also increases in the southern sections, for both small faults such as F30 and large faults such as F70 and F80 (Fig. 12).

Along the Z direction, deformation heterogeneities in the MDZ are related to the propagation of faults through subunits of different lithology. Subunits 2E to 2K are arranged in two slightly consolidated silty carbonate packages (subunits 2E to 2H and subunits 2J to 2K) separated by the clay-rich subunit 2I (Fig. 14a). Faults propagate upwards and downwards through the silty packages, and they are arrested at clay-rich subunit 2I, where slip is accommodated by folds near the fault tips (Fig. 14a).

Clay-rich subunits in the MDZ present a distinctive deformation style. The most remarkable is subunit 2I, which develops injection structures along faults and detachment levels, mostly in the eastern part of the MDZ (Fig. 6a-b). In these injections, 2I losses its internal lamination. Large fault-controlled clay injections such as those along F50 (Fig. 7) are heterogeneous along the vertical (Z) direction, as they are more extensive downwards (Fig. 9). In some cases, the deformation is so intense that subunit 2I is squeezed, ruptured and isolated (Fig. 6b). Here, subunit 2I is deformed by cm-scale faults (Fig. 14b), laterally grading into a chaotic breccia formed by internally laminated, rotated fragments surrounded by a clayish matrix (Fig. 14c), and the lamination is oblique to that of the underlying and overlying subunits (Fig. 14d). Clay-rich subunits 2I, 2K, and 2N act as detachment levels, allowing the formation of flat-ramp fault geometries, listric faults, horsts, grabens (Fig. 13c), and detachment folds (Fig. 14e). The gravel- and sand-rich subunit 2B in the western part of the MDZ also presents a distinctive behaviour. It is offset by minor faults in the N (Fig. 6a), while it is smeared towards WF southwards (Fig. 6b-c).

5. Discussion

The interpretation and correlation of the excavated sections and the derived 3D model of the fault zone provide valuable insight into the variability of fault zone architecture, styles of deformation, and fault zone evolution. The fault zone is the result of heterogeneous deformation, which produced a heterogeneous distribution of structures and deformation styles.

5.1. Fault zone architecture

In the fault zone, deformation is concentrated around the main fault strands WF and EF. Beds in the footwall and hanging wall damage zones of these faults are synthetic, i.e., they dip towards the downthrown block. This observation suggests a component of extensional folding associated with the propagation of these faults (Ferrill et al., 2005). The damage zone of WF is symmetrical. We interpret this symmetry as the result of a similar time span of deformation of units 1 (footwall) and 2 (hanging wall), since these units are similar in age (~2.8 Ma). On the other hand, the damage zone of EF is asymmetrical, with most of the deformation accumulated in the footwall (MDZ). We can also interpret this geometry in terms of the time span of deformation. Unit 2 in the middle block (~2.8 Ma) is older than unit 3 in the eastern block (~1.2-0.9 Ma). Consequently, unit 2 accumulated deformation over a longer period, resulting in a mature fault core and a more complex damage zone. The EF fault zone is thicker and more deformed than the WF fault zone. Since the throw of EF is approximately ten times larger than that of WF, this situation suggests a correlation between fault zone thickness and throw, as proposed by Evans (1990).

5.2. Deformation styles

One of the most interesting features of the studied sections is the variety of deformation styles that is documented at the outcrop scale. Faults record brittle deformation, while ductile deformation is expressed by folding, smearing, and clay fluidization (leading to total loss of the original clay internal structure and to clay injections). We postulate that the heterogeneous distribution of these different deformation styles was likely controlled by mechanical stratigraphy (Currie et al., 1962; Ferrill et al., 2017). To test this hypothesis, we compare the deformation styles of the different units with their mechanical stratigraphy. Units 1 to 3 consist of poorly lithified sediments, which were water-saturated when they were deformed

(Gibert et al., 2007a; García-Tortosa et al., 2008; Alfaro et al., 2010). However, these units have significant differences in mechanical stratigraphy: unit 1 (western block) primarily consists of thick beds of carbonate silts, unit 2 (MDZ) contains multi-layered alternations of thin layers of carbonate silts and clays with some thicker clay beds and gravels at the base, and unit 3 (eastern block) consists of carbonate silts interbedded with micrite limestones.

Unit 1 present in the western fault block is crosscut by cm- to m-throw faults and deformed by an anticline that developed in the WF footwall damage zone. Close inspection of the anticline forelimb reveals that bedding rotation is accommodated by sub-vertical minor (mm- to cm-throw) faults (Fig. 6). Thus, with the exception of clay smears from subunit 1G in the WF fault core, unit 1 mostly underwent brittle deformation.

A wide variety of deformation styles is observed in unit 2 of the MDZ. In the north-western part, a syncline was developed in the WF hanging wall damage zone (Fig. 6a). Close inspection shows that bedding rotation in the western limb of this syncline is accommodated by minor (mm- to cm-throw) faults. Synthetic and antithetic faults forming horst and graben structures are also present in the north-central part of the MDZ (Fig. 13c). Consequently, the western and central areas of the MDZ to the north experienced mostly brittle deformation. In the eastern part of the MDZ near EF, faults, bed rotation and thinning, clay smears and injections are all documented (Fig. 6a-b). These different deformation styles are the result of the multi-layered alternation of beds. Silty layers underwent brittle deformation, while clay-rich layers experienced ductile deformation.

In the western part of the MDZ, the sediments are mostly carbonate silts interbedded with thin clay levels (2A to 2H) and the coarser gravelly subunit 2B (Fig. 5). The predominance of silts and gravels led to more brittle deformation, although smears of H10 (including the gravelly sediments of subunit 2B) along WF (Fig. 6b), clay smears along minor faults, and minor folds are documented (Fig. 13 b-c).

The eastern part of the MDZ contains a larger number of clay-rich strata (subunits 2I, 2K, 2M and 2N). Therefore, ductile structures are more predominant here than in the western part. Silty subunits such as 2J and 2L underwent brittle deformation, while clay-rich subunits such as 2M and 2N were ductilely deformed (Fig. 6a). In section A3, a clay-rich bed acts as a detachment level, giving rise to a m-size detachment fold (Fig. 14e). In H30 on trench A0 (Fig. 6a), clay and silty beds of similar thickness are included in the EF fault core between high-throw faults F60 and F70. These beds are highly deformed, rotated, and thinned, and the silty beds accommodate extension by faulting, while clay beds accommodate extension by thinning and development of smears (Fig. 15; Sperrevik et al., 2000; Davatzes and Aydin, 2005). The result of this combination is stretched, silty beds sandwiched between clay smears (Fig. 15). Similar structures in siliciclastic interbedded sequences are described by Van der Zee et al. (2003), Davatzes and Aydin (2005), and Van der Zee and Urai (2005). With more fault displacement, the initially separated clay layers may be amalgamated into a single, thicker smear (Van der Zee et al., 2003; Van der Zee and Urai, 2005).

Mechanical stratigraphy within unit 2 controls fault propagation. Faults propagate through brittle silty layers that accommodate small amounts of pre-faulting strain, but the faults are arrested by ductile clay-rich layers, which can accommodate larger proportions of pre-faulting strain (Fig. 14a; Donath, 1970; Donath and Fruth, 1971; Ferrill and Morris, 2008). The bed thickness/fault throw ratio also plays an important role in fault propagation: thick clay beds are more effective for arresting faults than thin clay beds, and large-throw (> 1 m) faults are more prone to offset clay beds than low-throw faults. This contrast leads to more segmentation of the minor faults, while larger faults (e.g., F19 and F51) can offset subunit 2I (Fig. 13a-b).

Subunit 2I plays an important role in the deformation style of unit 2. This clayey subunit arrests fault propagation (Fig. 14a) and acts as a detachment level for larger faults such as F21 (A5, Fig. 6b). Together with clay-rich subunit 2K, 2I contributes to the stretching and boudinage of silty subunit 2J (Fig. 14a-b). However, the most remarkable feature of subunit 2I is its ability to flow. This property is evident from the internal structure of 2I combining both brittle and ductile deformation (Fig. 14b-d) and also from the injection structures of this unit along faults in the MDZ (Figs. 7 and 9). These features suggest that subunit 2I was characterized by different deformation styles. The overlying, laminated clay shows both brittle and ductile structures, whereas the underlying, massive clay shows fluid-like features. The lacustrine sediments in the trench were water-saturated during deformation (Gibert et al., 2007a; García-Tortosa et al., 2008; Alfaro et al., 2010). When the massive clay of subunit 2I underwent deformation, it may have experienced fluidization (sensu Allen, 1982; Owen, 1987) and upwards and lateral escape through the laminated clay. This process may have caused the collapse of the overlying laminated clay, producing fractures, tilted layers, and the observed laminated breccias surrounded by massive clay (Fig. 14b-d). Fluidized massive clay may have escaped upwards along fractures as injection structures cutting through the overlying units (e.g., F80 in A5, Fig. 6b). As clay escaped, it was squeezed laterally and even ruptured in some areas, putting it directly in contact the underlying and overlying subunits (Fig. 6b). The trigger mechanism for the clay fluidization is not clear. Some authors relate this phenomenon to seismic activity (Strachan, 2002; García-Tortosa et al., 2011). Although the Baza Fault is a seismogenic structure (Alfaro et al., 2008) and spectacular seismites have been described in the Baza sub-basin (Alfaro et al., 1997, 2010), further research is necessary to understand the formation of these structures.

Finally, the deformation of unit 3 in the eastern block is mainly characterized by a syncline against EF. This fold is well represented in the silty layers of unit 3, which are thinned progressively towards EF, possibly suggesting syn-growth (Fig. 6a-c). As in the western block, this fold is internally deformed by minor brittle structures that are more evident in the micritic limestone.

In conclusion, our observations indicate that the highly heterogeneous deformation styles described are the consequences of 1) poorly lithified and water-saturated sediments during deformation and 2) mechanical stratigraphy, as clay-rich lithologies are more likely to undergo ductile deformation, while silty, gravelly, and limestone lithologies are prone to brittle deformation.

5.3. Fault zone evolution

The WF and EF fault zones define the western, middle (MDZ) and eastern blocks. In the middle block (MDZ), the WF hanging wall damage zone, EF footwall damage zone and EF fault core coexist (Fig. 16a-b). The combined activity of these faults led to higher deformation and consequently a higher development of structures in the MDZ.

Several models for the development of normal fault zones have been proposed (Peacock and Sanderson, 1991 and 1994; Childs et al., 1996; Gabrielsen and Clausen, 2001; Kristensen et al., 2008; Childs et al., 2009, among others). In general, these models involve three main stages: 1) an initial stage in which faulting occurs on a series of segments characterized by surface irregularities; 2) a second stage in which the segments link by relay-ramp breaching or bypassing surface asperities, forming structures such as horses and duplexes; and 3) a final stage in which these structures are internally deformed, collapsed, and smeared along the fault. According to Gabrielsen and Clausen (2001), the fault zone widens during stages 1 and 2, while stage 3 causes fault zone thinning. On the other hand, Childs et al. (2009) suggest that fault zone thickness is strongly influenced from the first stage by the scale of the fault segmentation.

The MDZ is formed by a complex arrangement of rock bodies bounded by normal faults. Most of these rock bodies can be considered as horses forming an extensional duplex (sensu Gibbs, 1984; Childs et al., 1997). Moreover, some of the main horses show internal minor faults (Figs. 6a, 13a and 16c). According to these observations, we postulate that the MDZ was characterized by a mature stage of development, between stages 2 and 3 above, in which horses were stacked into duplexes and internally deformed. However, our observations point to a spatial variation in maturity along the Y (N-S) direction. In the northernmost trenches A00 to A2, some faults such as F10 and F11 present low angles and flat-ramp geometries, and the rock bodies are less deformed (I-I' in Fig. 16c). These fault surface irregularities indicate a less mature stage in the N, probably early stage 2. Southwards, in trenches A3 to A5, deformation in the horses increases; for instance, some minor faults such as F80 offset low-angle structures (II-II' in Fig. 16c), dividing H70 into new horses. We interpret these features as the beginning of asperity bifurcation, occurring during late stage 2. Finally, in the southernmost trenches B1-B3, horses are intensely deformed and smeared along fault surfaces, suggesting stage 3 of fault zone development (FIII-III' in Fig. 16c). Therefore, the MDZ becomes more mature southwards. This effect is strongly related to the convergence of WF and EF.

We interpret this spatial variation in maturity as a consequence of fault zone interaction. Two individual and well differentiated WF and EF fault zones can be observed ~100 m N of the study area (Fig. 16a). The fault zones are separated by a distance of ~100 m, and each zone is formed by a fault core and a damage zone. These fault zones gradually converge to the S towards the trench area, where their damage zones interact (Fig. 16b). This interaction increases southwards, from mild interaction leading to a less mature MDZ in trenches A00-A0 (Fig. 16b), to stronger interaction in trenches A2 to B1 leading to a more mature MDZ (II-II' in Fig. 16c). Finally, the strongest interaction occurs in trench B3, where the fault cores of WF and EF merge into a single fault core (III-III' in Fig. 16c), corresponding to a highly mature fault zone. We interpret this interaction as an "intersection damage zone" (sensu Peacock et al., 2017), a damage zone formed by the intersection of the kinematically linked WF and EF fault zones. This intersection is located between trenches B1 and B0 (Fig. 16b).

In terms of fault zone thickness, the MDZ seems to support the fault growth model of Childs et al. (2009), where the thickness of the MDZ is controlled by the geometry of the bounding WF and EF, rather than by fault evolution. The MDZ does not become thicker with more fault displacement to the south (Fig. 12) but actually becomes thinner because it is controlled by the WF and EF strands. The fault core, on the other hand, becomes thicker to the south because of the amalgamation of the WF and EF fault cores, giving rise to a single fault zone. Obliquely (β and γ) oriented faults (e.g., F40 and F50, Table 1) play an important role in accommodating the interaction of WF and EF, particularly where these two faults converge, deeper in the section and to the S (Figs. 9 and 16).

6. Conclusions and future work

Although not unexpected, it is interesting to see the difference between the surface exposure of the fault zone, and the excavated, fresh exposure. Poor exposure is certainly one of the reasons behind our simplistic conceptual models of fault zones (Schneeberger et al., 2017). The analysis, interpretation, and correlation of the excavated sections, together with the construction of a 3D model, have proven to be useful methods to understand the complex fault zone architecture and to some extent its evolution. This 4D picture of the fault zone dispels some of the myths about normal fault zones.

Faults are not surfaces but irregular fault zone volumes that are highly variable in 3D and over short distances (less than 1 m). Fault architecture, deformation styles, and fault facies are heterogeneous, which in our case is consequence of the variability in fault geometry, fault displacement, and mechanical stratigraphy. Differences in throw and time span of the bounding strands control the distribution of deformation across the fault zone (E-W direction) and thus the fault zone thickness and symmetry. Along-strike variations in the geometry of the bounding strands cause redistribution of deformation in the N-S direction. Southward convergence of WF and EF leads to increasing interaction of their fault zones, which is accommodated by secondary sub-parallel (α) and oblique fault strands (β and γ). This process increases the throw of bounding and internal faults and thus the maturity of the MDZ to the south. Where WF and EF interactions are maximum, their fault cores merge, giving rise to a single fault zone. Therefore, the evolutionary stage of the fault zone depends not only on the throw and the time elapsed since the onset of deformation but also on the geometric variations of the fault system. The development of the fault zone in poorly lithified, water-saturated, and multi-layered sediments leads to high heterogeneity in deformation styles: silty, gravelly, and limestone lithologies are prone to brittle deformation, while clay-rich lithologies are more likely to undergo ductile deformation and even fluidization. Mechanical stratigraphy also controls fault propagation. Facies within the fault zone (fault facies; Braathen et al., 2009) are heterogeneous. Coarse-grained, high-permeability facies (e.g., subunit 2B), and clay-rich, low-permeability facies (e.g., subunit 2I) are variable in three dimensions (Fig. 9). Smears along the fault zones are not homogeneous in either their lithology or their spatial distribution. Clays, silts, sands and gravels are all smeared along WF and EF. Clay injections favoured by sub-parallel or oblique (e.g., F50) fault conduits also accommodate fault zone deformation.

The studied fault zone is to some extent unique because it juxtaposes poorly consolidated sediments. Along the Baza Fault, other localities in lacustrine, soft sediments exhibit the same complexity, so from the structural point of view, there is nothing peculiar about the chosen site, other than the convergence of two bounding strands. One important question is how the fault zone varies with depth. One might expect less complexity as sediment compaction increases with depth, although some of the observed near-surface characteristics may still be present at greater depth (Childs et al., 1997; Vrolijk et al., 2016). The grain scale, microscopic structures and mechanisms of deformation, as well as a detailed chronology of deformation, are other important aspects that are not touched upon in this paper.

From a modelling perspective, one important question is how one may represent and upscale the fault zone structure for groundwater (Bense et al., 2013) and hydrocarbon flow models (Manzocchi et al., 2010). It is difficult to represent the observed fault zone heterogeneity at scales of metres to decametres, either through transmissibility multipliers (Manzocchi et al., 1999) or explicit volumetric fault facies representations (Fachri et al., 2016). One way to approach this problem is through seismic forward modelling (Lecomte et al., 2016) of the fault zone, which can deliver images at different frequencies and wavelengths. For other interesting sites along the Baza Fault, one could perform ground penetrating radar (GPR) and seismic acquisition before excavation, thus allowing a comparison between the outcrop and the geophysical image, as well as providing more information about fault deformation with depth. These issues are the subject of ongoing research.

Acknowledgements

In addition to the authors, Julia Castro (U. Alicante), Jacob Dieset (U. Stavanger), and Jan Tveranger (Uni Research) were also involved in the field campaign. We thank them for their active participation and constructive discussions. We also thank Escolástico Sánchez for his dexterity and patience in operating the bulldozer to excavate the trenches. Reviews by Fabrizio Agosta and an anonymous reviewer greatly improved the manuscript. We thank Midland Valley and Uni Research for allowing us to use their software packages Move and LIME, respectively, on an academic basis. The excavated sections, interpreted traces, and reconstructed horizons and faults are included in a LIME project. Anyone who wishes access to this project is welcome to contact the authors.

References

Agustí, J., Cabrera, L., Garces, M., Krijgsman, W., Oms, O. and Pares, J.M. 2001. A calibrated mammal scale for the Neogene of western Europe; state of the art. Earth-Science Reviews 52, 247-260.

Agosta, F., Mulch, A., Camberline, P. and Aydin, A. 2008. Geochemical traces of CO2 rich fluid flow along normal faults in central Italy. Geophysical Journal International 174, 758-770.

Alfaro, P., Moretti, M. and Soria, J.M. 1997. Soft-sediment deformation structures induced by earthquakes (seismites) in Pliocene lacustrine deposits (Guadix- Baza basin, Central Betic Cordillera). Eclogae Geol. Helv. 90, 531–540.

Alfaro, P., Delgado, J., Sanz de Galdeano, C., Galindo- Zaldívar, J., García-Tortosa, F.J., López-Garrido, A.C., López-Casado, C., Marín-Lechado, A., Gil, A. and Borque, M.J. 2008. The Baza Fault: a major active extensional fault in the central Betic Cordillera (south Spain). International Journal of Earth Sciences 97, 1353-1365.

Alfaro, P., Gibert, L., Moretti, M., García-Tortosa, F.J., Sanz de Galdeano, C., Galindo-Zaldívar, J. and López-Garrido, A.C. 2010. The significance of giant seismites in the Plio-Pleistocene Baza palaeo-lake (S. Spain). Terra Nova 22, 172–179.

Allen, J.R.L. 1982. Sedimentary structures: Their character and physical basis, Volume II. Elsevier, New York, 663 p.

Bense, V.F. and Van Balen, R.T. 2004. The effect of fault relay and clay smearing on groundwater flow patterns in the Lower Rhine Embayment. Basin Research 16, 397–411.

Bense, V. F. and Person, M.A. 2006. Faults as conduit-barrier systems to fluid flow in siliciclastic sedimentary aquifers. Water Resources Research 42, W05421, 1-18.

Bense, V.F., Gleeson, T., Loveless, S.E., Bour, O. and Scibek, J. 2013. Fault zone hydrogeology. Earth-Science Reviews 127, 171-192.

Braathen, A., Tveranger, J., Fossen, H., Skar, T., Cardozo, N., Semshaug, S.W., Bastesen, E. and Sverdrup, E. 2009. Fault facies and its application to sandstone reservoirs. AAPG Bulletin 93, 891-917.

Braathen, A., Osmundsne, P.T., Hauso, H., Semshaug, S., Fredman, N. and Buckley, S.J. 2013. Fault-induced deformation in a poorly consolidated, siliciclastic growth basin: A study from the Devonian in Norway. Tectonophysics 586, 112-129.

Caine, J.S., Evans J.P. and Forster, C.B. 1996. Fault zone architecture and permeability structure. Geology 24, 1025-1028.

Castro, J., Martin-Rojas, I., Medina-Cascales, I., García-Tortosa, F.J., Alfaro, P. and Insua-Arévalo, J.M. 2018. Active faulting in the central Betic Cordillera (Spain):

Palaeoseismological constraint of the surface-rupturing history of the Baza Fault (Central Betic Cordillera, Iberian Peninsula). Tectonophysics 736, 15-30.

Childs, C., Watterson, J. and Walsh, J.J. 1996. A model for the structure and development of fault zones. Journal of the Geological Society (London) 153, 337-340.

Childs, C., Walsh, J.J. and Watterson, J. 1997. Complexity in fault zone structure and implications for fault seal prediction. In: Møller-Pederson, P., Koestler, A.G. (eds.). Hydrocarbon Seals: Importance for Exploration and Production. NPF Special Publication 7, 61-72.

Childs, C., Manzocchi, T., Walsh, J.J., Bonson, C.G., Nicol, A. and Schöpfer, M.P.J. 2009. A geometric model of fault zone and fault rock thickness variations. Journal of Structural Geology 31, 117-127.

Currie, J.B., Patnode, H.W., Trump, R.P. 1962. Development of folds in sedimentary strata. Geological Society of America Bulletin 73, 655-673.

Davatzes, N.C. and Aydin, A. 2005. Distribution and Nature of Fault Architecture in a Layered Sandstone and Shale Sequence: An Example from de Moab Fault, Utah. In Sorkhabi R. and Tsuji Y. (eds.). Faults, fluid flow, and petroleum traps: AAPG Memoir 85, 153– 180.

Dockrill, B. and Shipton, Z.K. 2010. Structural controls on leakage from a natural CO2 geologic storage site: Central Utah, U.S.A. Journal of Structural Geology 32, 1769-1782.

Donath, F.A. 1970. Some information squeezed out of rock. American Scientist 58, 54-72.

Donath, F.A. and Fruth Jr., L.S. 1971. Dependence of strain-rate effects on deformation mechanism and rock type. Journal of Geology 79, 347-371.

Eichhubl, P., D'Onfro, S., Aydin, A., Waters, J. and McCarty, D.K. 2005. Structure, petrophysics, and diagenesis of shale entrained along a normal fault at Black Diamond Mines, California – Implications for fault seal. AAPG Bulletin 89, 1113-1137.

Eichhubl, P., Davatzes, N.C. and Becker, S.P. 2009. Structural and diagenetic control of fluid migration and cementation along the Moab fault, Utah. AAPG Bulletin 93, 653-681.

Evans, J. P. 1990. Thickness-displacement relationships for fault zones. Journal of Structural Geology 12, 1061-1065.

Fachri, M., Tveranger, J., Braathen, A. and Røe, P. 2016. Volumetric faults in field-sized reservoir simulation models: A first case study. AAPG Bulletin 100, 795-817.

Fairley, J.P. 2009. Modeling fluid flow in a heterogeneous, fault-controlled hydrothermal system. Geofluids 9, 153-166.

Faulkner, D.R., Jackson, C.A.L., Lunn, R.J., Shlische, R.W., Shipton, Z.K. and Wibberley, C.A.J. 2010. A review of recent developments concerning the structure, mechanics and fluid flow properties of fault zones. Journal of Structural Geology 32, 1557-1575.

Fernández-Ibáñez, F., Pérez-Peña, J.V., Azor, A., Soto, J.I. and Azañón, J.M. 2010. Normal faulting driven by denudational isostatic rebound. Geology, 38, 643-646.

Ferrill, D.A., Morris, A.P., Sims, D.W., Waiting, D.J. and Hasewaga, S. 2005. Development of synthetic layer dip adjacent to normal faults. In Sorkhabi, R. and Tsuji, Y. (eds.). Faults, fluid flow, and petroleum traps. AAPG Memoir 85, 125-138.

Ferrill, D.A. and Morris, A.P. 2008. Fault zone deformation controlled by carbonate mechanical stratigraphy, Balcones fault system, Texas. AAPG Bulletin 92, 359-380.

Ferrill, D.A., Morris, A.P., McGinnis, R.N., Smart, K.J., Wigginton, S.S. and Hill, N.J. 2017. Mechanical stratigraphy and normal faulting. Journal of Structural Geology 94, 275-302.

Folch, A. and Mas-Pla, J. 2008. Hydrogeological interactions between fault zones and alluvial aquifers in regional flow systems. Hydrological Processes 22, 3476–3487.

Fossen, H., Johansen, T.E.S., Rotevatn, A. and Hesthammer, J., 2005. Fault interaction in porous sandstones. AAPG Bulletin 89, 1593-1606.

Foxford, K.A., Walsh, J.J., Watterson, J., Garde, I.R., Guscott, S.C. and Burley, S.D. 1998. Structure and content of the Moab Fault zone, Utah, USA, and its implications for fault seal prediction. In Jones, G., Fisher, Q.J. and Knipe, R.J. (eds.). Faulting, Fault Sealing and Fluid Flow in Hydrocarbon Reservoirs. Geological Society (London), Special Publications 147, 87-103.

Gabrielsen, R.H. and Clausen, J.A. 2001. Horses and duplexes in extensional regimes: A scale modeling contribution. In: Koyi, H.A. and Mancktelow, N.S. (eds.). Tectonic Modeling: A Volume in Honor of Hans Ramberg. Geological Society of America Memoirs 193, 219-233.

Gabrielsen, R. H., Braathen, A., Kjemperud, M. and Valdresbråten, M. L. R. 2017. The geometry and dimensions of fault-core lenses. In Childs, C. et al. (eds.). The Geometry and Growth of Normal Faults. Geological Society (London), Special Publications 439, 249-269.

Galindo-Zaldívar, J., Jabaloy, A., Serrano, I., Morales, J., González-Lodeiro, F. and Torcal, F. 1999. Recent and present-day stresses in the Granada Basin (Betic Cordilleras): Example of a late Miocene-present-day extensional basin in a convergent plate boundary. Tectonics 18, 686-702.

García Tortosa, F.J., Alfaro, P., Galindo Zaldívar, J., Gibert, L., López Garrido, A.C., Sanz de Galdeano, C. and Ureña, M. 2008. Geomorphologic evidence of the active Baza fault (Betic Cordillera, South Spain). Geomorphology 97, 374-391.

García Tortosa, F.J., Alfaro, P., Galindo Zaldívar J. and Sanz de Galdeano, C. 2011. Glacis geometry as a geomorphic marker of recent tectonics: the Guadix-Baza Basin (South Spain). Geomorphology 125, 517-529.

García-Tortosa, F.J., Alfaro, P., Gibert, L. and Scott, G. 2011. Seismically induced slump on an extremely gentle slope (<1°) of the Pleistocene Tecopa paleolake (California). Geology 39 (11), 1055- 1058.

Gibbs, A.D. 1984. Structural evolution of extensional basin margins. Journal of the Geological Society (London) 141, 609-620.

Gibert, L., Ortí, F. and Rosell, L. 2007a. Plio-Pleistocene lacustrine evaporites of the Baza Basin (Betic Chain, SE Spain). Sedimentary Geology 200, 89-116.

Gibert, L., Scott, G., Martin, R. and Gibert, J. 2007b. The early to middle Pleistocene boundary in the Baza basin (Spain). Quaternary Science Reviews 26, 2067-2089.

Grauls, D., Pascaud, F. and Rives, T. 2002. Qualitative fault seal assessment in hydrocarbon-compartmentalized structures using fluid pressure data. In Koestler, A.G., Hunsdale, R. (eds.). Hydrocarbon Seal Quantification. Norwegian Petroleum Society, Special Publications 11, 141-156.

Gray, M. B., Stamatakos, J. A. Ferrill, D. A. and Evans, M. A. 2005. Fault-zone deformation in welded tuffs at Yucca Mountain, Nevada, USA. Journal of Structural Geology 27, 1873-1891.

Haberland, C., Giber, L., José Jurado, M., Stiller, M. et al. 2017. Architecture and tectono-stratigraphic evolution of the intramontane Baza Basin (Bétics, SE-Spain): Constraints from seismic imaging. Tectonophysics 709, 69-84.

Heynekamp, M.R., Goodwin, L.B., Mozley, Ps.S. and Haneberg, W.C. 1999. Controls on fault-zone architecture in poorly lithified sediments, Rio Grande Rift, New Mexico: Implications for fault zone permeability and fluid flow. In Haneberg, P.S., Mozley, P.S., Moore, J.C. and Goodwin, L.B. (eds.). Faults and Subsurface Fluid Flow in the Shallow Crust. American Geophysical Union Monograph 113, Washington, 27-49.

Kettermann, M., Thronberens, S., Juarez, O., Urai, J.L., Ziegler, M., Asmus, S. and Krüger, U. 2016. Mechanisms of clay smear formation in unconsolidated sediments – insights from 3-D observations of excavated normal faults. Solid Earth 7, 789-815.

Kim, Y.-S., Peacock, D.C.P. and Sanderson, D.J. 2004. Fault damage zones. Journal of Structural Geology 26, 503-517.

Kristensen, M., Childs, C. and Korstgard, J. 2008. The 3D geometry of small-scale relay zones between normal faults in soft sediments. Journal of Structural Geology 30, 257–272.

Kristensen, M.B., Childs, C., Olesen, N.O. and Korstgard, J.A. 2013. The microstructure and internal architecture of shear bands in sand-clay sequences. Journal of Structural Geology 46, 129-141.

Laubach, S.E., Eichhubl, P., Hilgers, C. and Lander, R.H. 2010. Structural diagenesis. Journal of Structural Geology 32, 1866-1872.

Lecomte, I., Lavadera, P.L., Botter, C., Anell, I., Buckley, S., Haug Eide, C., Grippa, A., Mascolo, V. and Kjoberg, S. 2016. 2(3)D convolution modelling of complex geological targets beyond - 1D convolution. First Break 34, 99–107.

Lehner, F.K. and Pilaar, W.F. 1997. The emplacement of clay smears in synsedimentary normal faults: inferences from field observations near Frechen, Germany. In Møller-Pedersen, P., Koestler, A.G. (eds.). Norwegian Petroleum Society Special Publications: Hydrocarbon Seals: Importance for Exploration and Production. Elsevier Science, 39-50.

Loveless, S., Bense, V. and Turner, J. 2011. Fault architecture and deformation processes within poorly lithified rift sediments, Central Greece. Journal of Structural Geology 33, 1554-1568.

Manzocchi, T., Walsh, J.J., Nell, P. and Yielding, G. 1999. Fault transmissibility multipliers for flow simulation models. Petroleum Geoscience 5, 53–63.

Manzocchi, T., Childs, C., andWalsh, J. 2010. Faults and fault properties in hydrocarbon flow models. Geofluids 10, 94-113.

Martínez-Solares, J.M. and Mezcua, J. 2003. Catálogo sísmico de la Península Ibérica (880 AC-1900). Inst. Geogr. Nac. (Madrid), 254 pp.

Ofoegbou, G.I., Painter, S., Chen, R., Randall, W.F. and Ferril, D.A. 2001. Geomechanical and thermal effects on moisture flow at the proposed Yucca mountain nuclear waste repository. Nuclear Technology 134, 241–262.

Owen, G. 1987. Deformation processes in unconsolidated sands. In: Jones, M.E., Preston, R.M.F. (Eds), Deformation of Sediments and Sedimentary Rocks. Geological Society, London, Special Publication 29, 11-24.

Peacock, D.C.P. and Sanderson, D.J. 1991. Displacements, segment linkage and relay ramps in normal fault zones. Journal of Structural Geology 13, 721-733.

Peacock, D.C.P. and Sanderson, D.J. 1994. Geometry and Development of Relay Ramps in Normal Fault Systems. AAPG Bulletin 78, 147-165.

Peacock, D.C.P., Dimmen, V., Rotevatn, A. and Sanderson, D.J. 2017. A broader classification of damage zones. Journal of Structural Geology 102, 179-192.

Person, M., Banerjee, A., Hofstra, A., Sweetkind, D. and Gao, Y. 2008. Hydrologic models of modern and fossil geothermal systems in the Great Basin: genetic implications for epithermal Au–Ag and Carlin-type gold deposits. Geosphere 4, 888-917.

Peña, J.A. 1985. La Depresión de Guadix-Baza. Estudios Geológicos 41, 33-46.

Pla-Pueyo, S., Viseras, C., Soria, J.M., Tent-Manclús, J.E. and Arribas, A. 2011. A stratigraphic framework for the Pliocene–Pleistocene continental sediments of the Guadix Basin (Betic Cordillera, S. Spain). Quaternary International 243, 16-32.

Rawling, G.C. and Goodwin, L.B. 2006. Structural record of the mechanical evolution of mixed zones in faulted poorly lithified sediments, Rio Grande rift, New Mexico, USA. Journal of Structural Geology 28, 1623-1639.

Rice, J.R. and Cocco, M. 2007. Seismic fault rheology and earthquake dynamics. In: Handy, M.R., Hirth, G., Hovious, N. (eds.). The Dynamics of Fault Zones, 99-137. MIT Press, Cambridge, MA.

Rowland, J.V. and Sibson, R.H. 2004. Structural controls on hydrothermal flow in a segmented rift system, Taupo Volcanic Zone, New Zealand. Geofluids 4, 259-283.

Sanz de Galdeano, C., García-Tortosa, F.J., Peláez, J.A., Alfaro, P., Azañón, J.M., Galindo-Zaldívar, J., López-Casado, C., López-Garrido, A.C., Rodríguez-Fernández, J. and Ruano, P. 2012. Main active faults in the Granada and Guadix-Baza Basins (Betic Cordillera). Journal of Iberian Geology 38, 209-223.

Schneebergeer, R., La Varga, M., Egli, D., Berger, A., Kober, F., Wellmann, F. and Herwegh, M. 2017. Methods and uncertainty estimations of 3-D structural modelling in crystalline rocks: a case study. Solid Earth, 987-1002.

Scholz, C.H. 2002. The mechanics of Earthquakes and Faulting. Cambridge University Press, Cambridge.

Shipton, Z.K. and Cowie, P.A. 2001. Damage zone and slip-surface evolution over [mu]m to km scales in high-porosity Navajo sandstone, Utah. Journal of Structural Geology 23, 1825-1844.

Shipton, Z.K. and Cowie, P.A. 2003. A conceptual model for the origin of fault damage zone structures in high-porosity sandstone. Journal of Structural Geology 25, 333-344.

Shipton, Z., Evans, J., Kirchner, D., Kolesar, P., Williams, A. and Heath, J. 2004. Analysis of CO_2 leakage through low-permeability faults from natural reservoirs in the Colorado Plateau, southern Utah. In: Baines, S., Worden, R. (eds.), Geological Storage of Carbon Dioxide. Geological Society (London), Special Publications 233, 43–58.

Sibson, R.H. 1986. Earthquakes and rock deformation in crustal fault zones. Annual Review of Earth and Planetary Sciences 14, 149-175.

Sibson, R.H. 2003. Thickness of the seismic slip zone. Bulletin of the Seismological Society of America 93, 1169-1178.

Solum, J.G., Davatzes, N.C. and Lockner, D.A. 2010. Fault-related clay authigenesis along the Moab Fault: Implications for calculations of fault rock composition and mechanical and hydrologic fault zone properties. Journal of Structural Geology 31, 1899-1911.

Sorkhabi, R. and Tsuji, Y. 2005. Faults, Fluid Flow and Petroleum Traps. AAPG Memoir 85.

Sperrevik, S., Faerseth, R.B., Gabrielsen, R.H. 2000. Experiments on clay smear formation along faults. Petroleum Geoscience 6, 113-123.

Strachan. L.J. 2002. Slump-initiated and controlled syndepositional sandstone remobilization: An example from the Namurian of County Clare, Ireland. Sedimentology 49, 25-41.

Van der Zee, W., Urai, J.L. and Richard, P.D. 2003. Lateral clay injection into normal faults. GeoArabia 8, 501-522.

Van der Zee, W. and Urai, J.L. 2005. Processes of normal fault evolution in a siliciclastic sequence: a case study from Miri, Sarawak, Malaysia. Journal of Structural Geology 27, 2281-2300.

Vera, J. 1970. Facies del Plioceno de la Depresión de Guadix-Baza. Cuad. Geol. Univ. Granada 1, 23-25.

Viseras, C. 1991. Estratigrafía y sedimentología del relleno aluvial de la Cuenca de Guadix (Cordilleras Béticas). Tesis Doctoral, Universidad de Granada, España, 327 pp.

Vrolijk, P.J., Urai, J.L. and Kettermann, M. 2016. Clay smear: Review of mechanisms and applications. Journal of Structural Geology 86, 95-152.

Wibberley, C.A.J., Yielding, G. and Di Toro, G. 2008. Recent advances in the understanding of fault zone internal structure: a review. In Wibberley, C.A. et al. (eds.). The Internal

Structure of Fault Zones: Implications for Mechanical and Fluid Flow Properties. Geological Society (London), Special Publications 299, 5-33.

Wibberley, C.A.J., Gonzalez-Dunia, J. and Billon, O. 2017. Faults as barriers or channels to production-related flow: Insights from case studies. Petroleum Geoscience 23, 134-147.

Figure Captions

Figure 1. Geologic map of the Baza Fault and the Guadix-Baza Basin. Rectangle indicates the study area (Fig. 2). Inset shows the location of the basin in south-central Spain.

Figure 2. a. Geologic map of the Baza Fault in the study area. Red line shows the line of the section in b, and the rectangle shows the area around the Carrizal strand (Fig. 4a). **b.** Cross section ~ 500 m north of the excavated area. Left tick labels are metres above sea level. Cross section has no vertical exaggeration.

Figure 3. a. Map of the 13 trenches; bars indicate trench facing direction. EF and WF traces are also included. **b.** Interpreted photomosaic of trench A5. **c.** Trench A5 and floor photomosaics draped over the LiDAR data. Interpretation of A5 is also included. **d.** Interpolated F0 surface (red) containing the F0 traces on the trenches and the floor (red dashed lines). Trenches A1, A5 and floor are included. In c and d, the red arrow indicates N, and the floor section is ~ 15 m wide.

Figure 4. a. Simplified geological map of the study area. The east fault (EF) is the Carrizal fault, and the western fault (WF) is a secondary strand. Grey shading represents the fault zones. The black rectangle shows the trench area, and the red line marks the location of the section in c. **b.** Simplified scheme of the outcrop structure showing WF and EF, main blocks (W, middle and E), units (1 to 3) and subunits, faults (denoted by the letter F), and rock

bodies (denoted by the letter H). **c.** Detailed section based in the northernmost trench A00. The region between WF and EF is the main deformation zone (MDZ). Light grey transparent area is covered and its interpretation is based on the exposed area above. Cross section has no vertical exaggeration.

Figure 5. Stratigraphic column showing the subunits cropping out in the western (W) block (unit 1), main deformation zone (MDZ, unit 2), and eastern (E) block (unit 3). Right profiles of subunit blocks indicate relative competence (convex is more competent and vice versa).

Figure 6. Interpretations of E-W trenches **a.** A0, **b.** A5, and **c.** B3. Subunit colours and labels are as in Fig. 5. F stands for faults and H for rock bodies. Lower left inset shows the locations of the trenches. Photomosaics and interpretations of all trenches are included in the supplementary material.

Figure 7. Interpretation of the floor of the excavation between trenches A1 and B3. Subunit colours and labels are as in Fig. 5. F stands for faults and H for rock bodies. Inset shows the fault families α, β and γ (Table 1). Aerial photo and interpretation of the floor are included in the supplementary material.

Figure 8. Graphical summary of the correlation of subunits, faults (F), and rock bodies (H) between the trenches. Subunit colours and labels are as in Fig. 5. Numbers next to throw symbols are fault throw in m (red) and maximum fault infill thickness (black). Faults without a throw value have a throw greater than the trench height (> 4 m). Inset beside the legend shows the trenches locations. Photomosaics and interpretations of all trenches are included in the supplementary material.

Figure 9. Horizontal slices through the 3D model of the fault zone at **a.** 0.5 m, **b.** 1.5 m, **c.** 2.5 m, **d.** 3.5 m, and **e.** 4.5 m below the ground. Faults are denoted by F and rock bodies by H.

Subunit colours and labels are as in Fig. 5. Grey E-W lines are trenches A1 to B3. **f.** 3D fault framework and slices a to e.

Figure 10. Block diagram of the fault zone and its different faults (F) and rock bodies (H). Rock bodies are divided into W (light blue to light green), MDZ (dark green to red) and E (grey) block bodies. In the MDZ, the black bands along the faults represent clay from subunit 2I. The dotted pattern in H10 represents the gravels from subunit 2B.

Figure 11. 3D view of key fault splays in the fault zone. **a.** WF and EF, **b.** F3 and WF, **c.** WF and F10 to F30, **d.** F10, F40, F60, F70 and EF, **e.** F10 to F30 and F80, and **f.** F10 to F50 and F80.

Figure 12. Throw distribution of fault splays in the fault zone. Note that throws are grouped into measurable (less than excavation height) and not measurable (greater than excavation height) values. Distance is measured from northernmost trench A00 (Fig. 3a). Lowermost wedge schematically shows the thinning of the fault zone from ~7 m in the north to ~1 m in the south.

Figure 13. Closeups and interpretations of **a.** Middle sector of A3, **b.** Eastern, lower sector of A4, and **c.** Central, lower sector of A2. Subunit colours and labels are as in Fig. 5. F stands for faults and H for rock bodies. Distance between the white markers is 1 m. Sectors are shown on the photomosaics of the trenches in the supplementary material.

Figure 14. Closeups of **a.** Middle, lower sector of A2, **b.** Middle, central sector of A4, **c-d.** Red rectangles in b, and **e.** Eastern sector of A3. In e, distance between the white markers is 1 m. Sectors a and b are shown on the photomosaics of the trenches in the supplementary material.

Figure 15. Closeups of the eastern sector of A0. **a.** Photo, **b.** Interpretation. Strata are coloured following the legend at the bottom. Note that the silty beds are sandwiched between the clay smears. Sector is shown on the photomosaic of the trench in the supplementary material.

Figure 16. Interaction of the WF and EF fault zones. **a.** Geological map of the study area, **b.** Detailed map illustrating the interaction of the fault zones, **c.** Cross sections I-I', II-II' and III-III' across the fault zones. Lines of sections are indicated in b. In b and c, fault zone elements are coloured according to the legend at the bottom.

Table 1. Summary of major faults, their geometries, and infills. For the description of fault smears and lenses, we use the classification schemes of Braathen et al. (2009, their Figs. 4 and 5).

Table 2. Summary of rock bodies, their boundaries, stratigraphies, and deformation.

Supplementary material

SM1. Photomosaics and interpretations of trenches **a.** A00 and **b.** A0. Subunit colours and labels are as in Fig. 5. F stands for faults and H for rock bodies. Inset shows the locations of the trenches. In b, dashed rectangle on photomosaic indicates the extent of Fig. 15.

SM2. Photomosaics and interpretations of trenches **a.** A1 and **b.** A2. Subunit colours and labels are as in Fig. 5. F stands for faults and H for rock bodies. Inset shows the locations of the trenches. In b, dashed rectangles on photomosaic indicate the extents of Figs. 13c and 14a.

SM3. Photomosaics and interpretations of trenches **a.** A3 and **b.** A4. Subunit colours and labels are as in Fig. 5. F stands for faults and H for rock bodies. Inset shows the locations of the trenches. In a and b, dashed rectangles on photomosaic indicate the extents of Figs. 13a-b and 14b, e.

SM4. Photomosaics and interpretations of trenches **a.** A5 and **b.** B0. Subunit colours and labels are as in Fig. 5. F stands for faults and H for rock bodies. Inset shows the locations of the trenches.

SM5. Photomosaics and interpretations of trenches **a.** C1, **b.** C2 and **c.** C3. Contrary to the other trenches, these trenches are parallel to EF, allowing the exposure of faults oblique to EF (e.g., F1). Subunit colours and labels are as in Fig. 5. F stands for faults and H for rock bodies. Inset shows the locations of the trenches.

SM6. Photomosaics and interpretations of trenches **a.** B1 and **b.** B3. Subunit colours and labels are as in Fig. 5. F stands for faults and H for rock bodies. Inset shows the locations of the trenches.

SM7. Drone aerial photo and interpretation of the floor of the excavation between trenches A1 and B3. Subunit colours and labels are as in Fig. 5. F stands for faults and H for rock bodies.

Fault	Fault geometry						Fault infill			
	Sections	Strike*1	Family	Dip*1	Throw	Shape	Type	Shape	Thickness	Source subunits
F1	B0-B3, C1, floor	~285°	β	50-85° N	0.3- 2 m	Planar	-	-	-	-
F2	A0, A2-B1, floor	~330°	α	60-85° E	0.2 - 1.4 m	Planar	clay smear	continuous-semicontinuous	mm	1D
F3	A00-B3, C2, floor	300-330°	α and β	~55° E	1.2 - > 4 m*2	Planar, Irregular	clay smear	continuous-semicontinuous	mm - ~5 cm	1D, 1G
WF	A00-B3, C2, floor	300-330°	α and β	~60° E	10s of meters*3	Planar	sand, clay and micrite breccia	continuous-semicontinuous	mm - ~20 cm	1A-1G, 2A – 2C
F11	A0	-	-	30-45° E	0.9 m	Ramp-flat-ramp	-	-	-	-
F12	B0, C2	~310°	β	~60° E	0.2 - 1.1 m	Irregular	-	-	-	-
F10	A00-A5, C3, floor	~340°	α	45-90° E	0.3 - 1.5 m	Planar, flat-ramp, listric	clay smear	ruptured	mm - ~4 cm	2E – 2H
F19	A3	-	-	85-90° E	0.6 m	Planar	clay smear	semicontinuous	mm	2J – 2K
F20	A2-A5, C3	~335°	α	70-90° W	0.2 - 2.7 m	Irregular	clay smear	continuous-ruptured	mm - ~5 cm	2E – 2K
F21	A4-A5	~335°	α	~45° E	1 m	Planar, irregular	clay smear	semicontinuous	mm - ~5 cm	2J – 2L
F22	A00-A1, floor	~310°	β	50-70° E	0.4 - 0.6 m	Planar, flat-ramp	clay smear	semicontinuous	mm - ~4 cm	2E – 2G, 2K
F30	B0-B3, floor	~300°	β	70°E - 70°W	> 4 m*2	Irregular	clay and sand smear	continuous	mm - ~13 cm	2C, 2D, 2K
F31	B0, floor	290-310°	β	-	> 4 m*2	Ramp-flat	-	-	-	-
F40	Floor	~290°	β	~85° SW	?	Planar	-	-	-	-
F50	A5, C3, floor	~220°	γ	~80° S	1. 5 m	Irregular	clay and micrite breccia	continuous	~3 - ~10 cm	2F – 2K
F51	A2-A4	~220°	γ	35-45° W	0.5 m	Planar, irregular	clay smear	continuous	~1 - ~4 cm	2K
F60	A0-A1	~320°	α	~60° E	> 4 m*2	Planar, Irregular	clay smear	continuous	mm - ~8 cm	2I
F70	A00-A1, floor	~320°	α	~60° E	> 4 m*2	Planar	clay smear	continuous-semicontinuous	mm - ~8 cm	2I
F79	A5-B0, floor	~330°	α	70-90° E	> 4 m*2	Flat-ramp	clay smear	ruptured	mm - ~4 cm	-
F80	A2-B3, floor	~340°	α	40-60° E	> 4 m*2	Flat-ramp, planar	clay smear	semicontinuous-ruptured	mm - ~5 cm	2M
EF	A00-B3, floor	~330°	α	~60° E	100s of meters*3	Planar, irregular	clay smear	semicontinuous-ruptured	mm - ~4 cm	2I, 2N

*1 Faults strikes and dips are calculated from 3D model. *2 Throw higher than trench depth (4m). *3 Estimated throw based on stratigraphy.

Fault block	Unit	Rock bodies		Boundaries	subunits	Inner deformation	Sections
Western Block	Unit 1	H1		F1, F2	1A-1C	Preserved bedding	B3, floor
		H2		F1, F2	1A-1E	Preserved bedding, offset by minor faults	C1, B0-B3, floor
		H3		F1, F2	1A-1E	Preserved bedding, offset by minor faults, smeared by F2	A0, A2-A5, C1, B0, floor
		H4		F1, F2, F3	1A-1G	Preserved bedding, offset by minor faults, smeared by F3	A00-A5, C2, B0-B3, floor
		H5		F3, WF	1C-1H	Offset by minor faults, stretched and smeared by WF; strongly deformed in B1-B3 sections	A00-A5, C2, B0-B3, floor
Main Deformation Zone (MDZ)	Unit 2	Western Set	H10	F10, F11, F12, F30	2A-2G	Stretched by WF and offset by minor faults; completely smeared by WF in A3-A5 and B3 sections	A00-A5, C2-C3, B0-B3, floor
			H11	WF, F12	2A-2D	Stretched and smeared by WF, offset by minor faults	C2, B0
			H12	F10, F11	2C-2E	Tilted to the W and offset by minor faults	A0
		Northern Set	H20	F10, F22, F40, F60	2D-2I	Preserved bedding, offset by minor faults; stretched by F60 in A00	A00-A1, floor
			H21	F22, F40, F60	2F-2H	Offset by minor faults, stretched and smeared by F60	A0-A1
			H30	F40, F60, F70	2J-2L	Strongly stretched and smeared	A00-A1, floor
			H40	F70, EF	2K-2N	Strongly stretched, folded and smeared	A00-A1, floor
		Central Set	H50	F10, F19, F20	2C-2K	Bedding preserved, tilted to the E, offset by minor faults	A2-A5, C3
			H51	F19, F20	2F-2K	Tilted to the E, smeared by F19	A3
			H60	F20, F50, Subunit 2I	2E-2H	Preserved bedding, tilted to the E, offset by minor faults, horst-graben, smeared by F10	A2-A5, floor
			H61	F20, F21, F50, F51, Subunits 2I and 2K	2J	Offset by minor faults, stretched, smeared by F20	A2-A5, floor
			H70	F20, F21, F50, F51, Subunit 2K	2K-2L	Preserved bedding, tilted to the E, offset by minor faults, horst-graben, smeared by F20	A2-A5, C3
		Southern Set	H79	F30, F31, F79, F80	2J?	Preserved bedding, tilted to the E, offset by minor faults	B0-B3, floor
			H80	F30, F31, F79, F80	2K-2L	Offset by minor faults, ductile structures, smeared by F30 and F80	A5, B0-B3, floor
			H81	F79, F80	2M	Offset by minor faults and stretched into lensed bodies, ductile structures, smeared along F80	A5, B0, floor
		Eastern Set	H90	F80, EF, 2I injection	2M	Offset by minor faults, ductile structures, stretched and smeared by EF	A2-A5
			H91	EF, 2I injection	2N	Ductile structures, strongly stretched and smeared by EF; detachment fold in A3	A2-A5
			H92	F80, EF	2M-2N	Ductile structures, strongly stretched and smeared by EF	B0-B3, floor
Eastern Block	Unit 3			EF		Preserved bedding, syncline against EF	A00-A5, B0-B3, floor

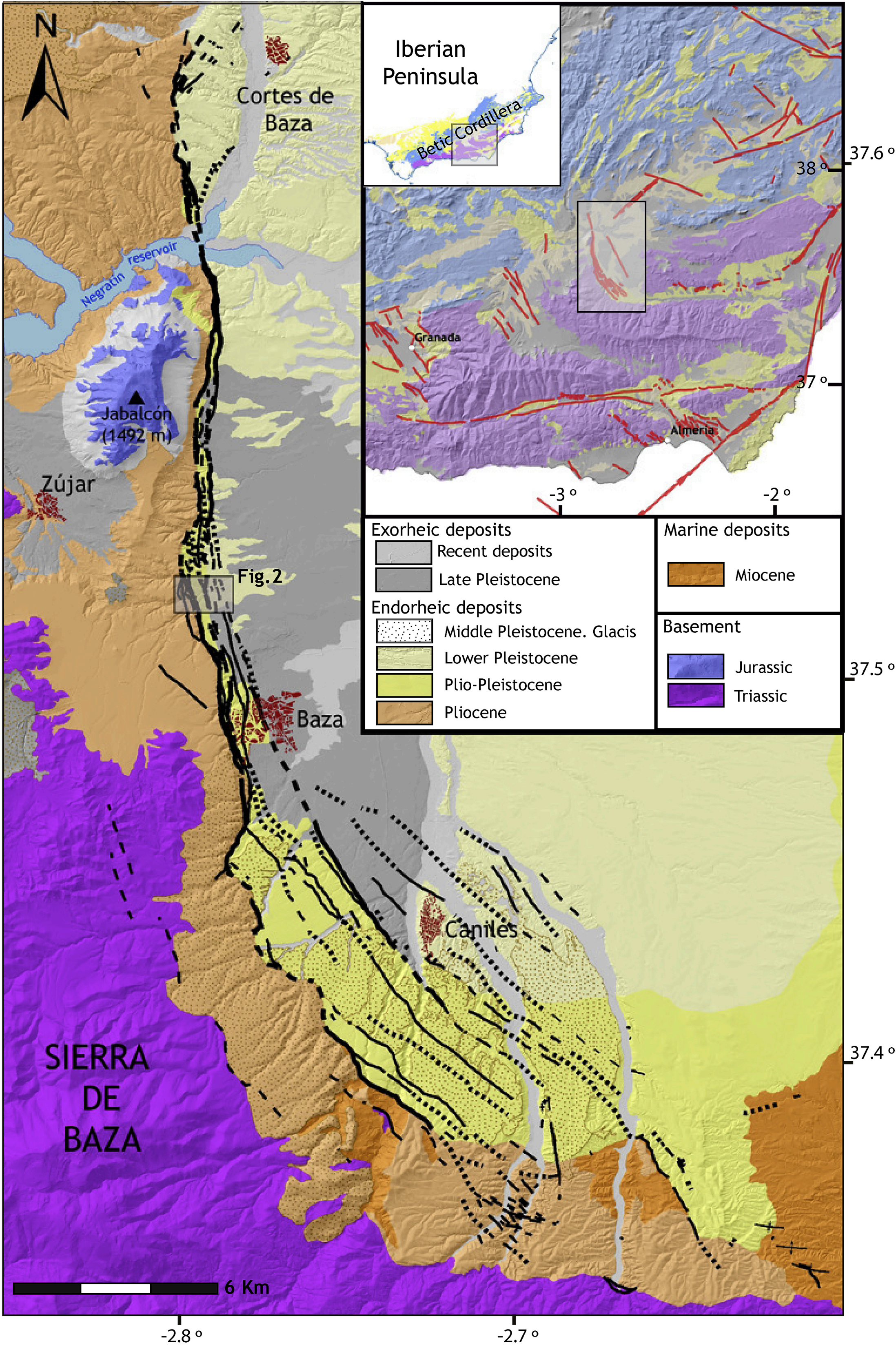
N
Cortes de Baza
Negratín reservoir
Jabalcón (1492 m)
Zújar
Fig.2
Baza
Caniles
SIERRA DE BAZA
6 Km
Iberian Peninsula
Betic Cordillera
Granada
Almeria
38 º
37 º
-3 º
-2 º
37.6 º
37.5 º
37.4 º
-2.8 º
-2.7 º
Exorheic deposits
Recent deposits
Late Pleistocene
Endorheic deposits
Middle Pleistocene. Glacis
Lower Pleistocene
Plio-Pleistocene
Pliocene
Marine deposits
Miocene
Basement
Jurassic
Triassic

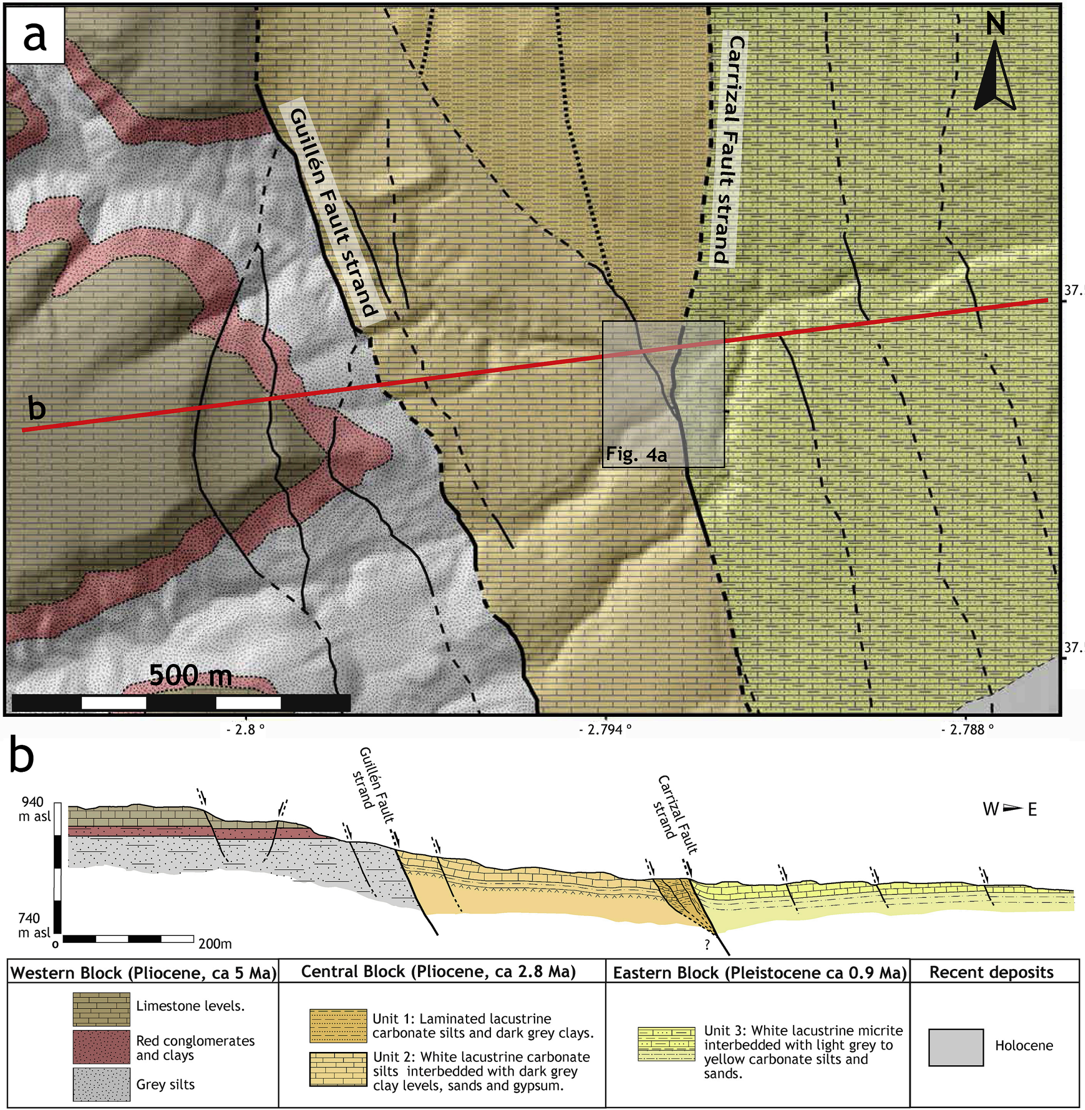
a
N
Guillén Fault strand
Carrizal Fault strand
Fig. 4a
b
500 m
37.521 °
37.516 °
- 2.8 °
- 2.794 °
- 2.788 °
b
940 m asl
740 m asl
0
200m
Guillén Fault strand
Carrizal Fault strand
?
W E
Western Block (Pliocene, ca 5 Ma)
Limestone levels.
Red conglomerates and clays
Grey silts
Central Block (Pliocene, ca 2.8 Ma)
Unit 1: Laminated lacustrine carbonate silts and dark grey clays.
Unit 2: White lacustrine carbonate silts interbedded with dark grey clay levels, sands and gypsum.
Eastern Block (Pleistocene ca 0.9 Ma)
Unit 3: White lacustrine micrite interbedded with light grey to yellow carbonate silts and sands.
Recent deposits
Holocene

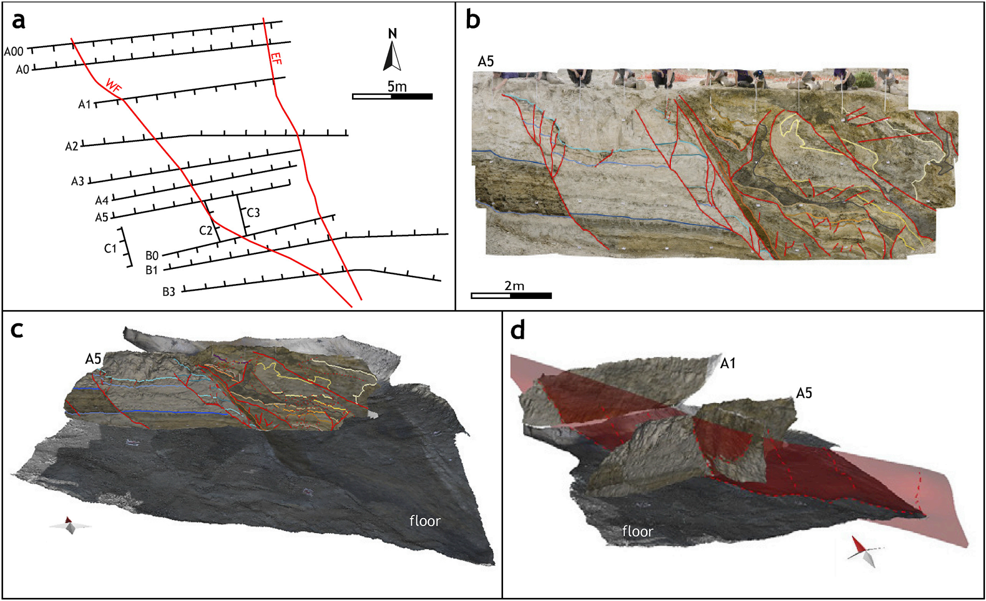
a
N
5m
A00
A0
A1
A2
A3
A4
A5
C1
C2
C3
B0
B1
B3
WF
EF
b
A5
2m
c
A5
floor
d
A1
A5
floor

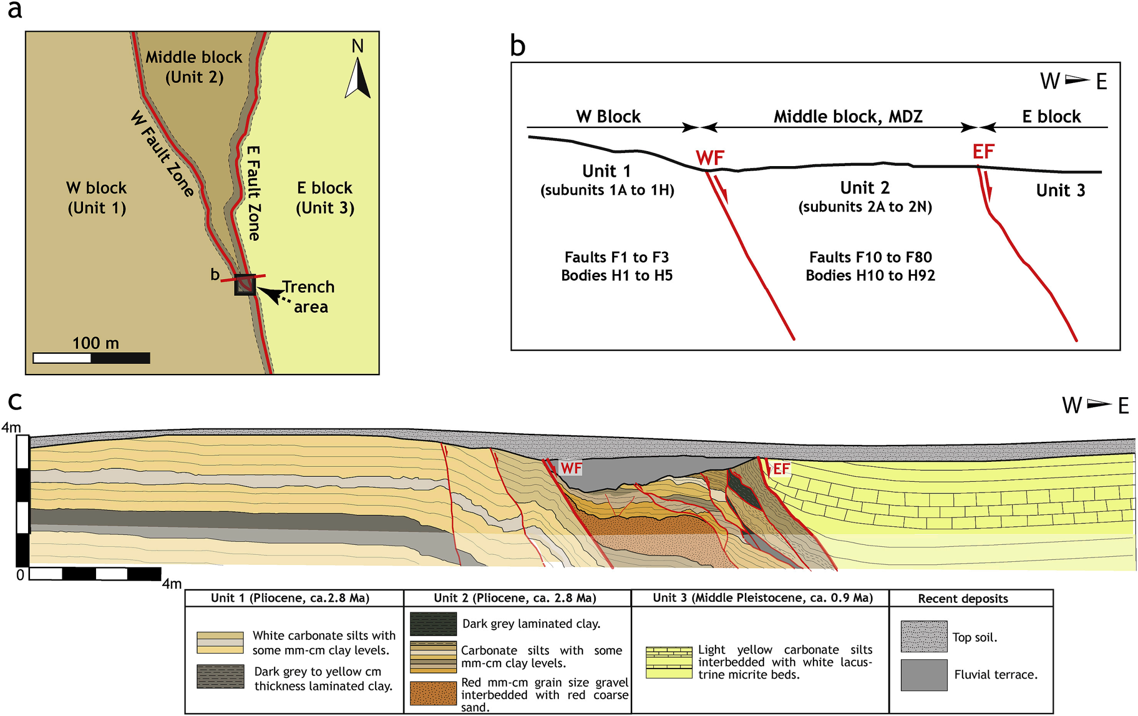
a
Middle block
(Unit 2)
N
W Fault Zone
E Fault Zone
W block
(Unit 1)
E block
(Unit 3)
b
Trench
area
100 m
b
W ► E
W Block
Middle block, MDZ
E block
WF
EF
Unit 1
(subunits 1A to 1H)
Unit 2
(subunits 2A to 2N)
Unit 3
Faults F1 to F3
Bodies H1 to H5
Faults F10 to F80
Bodies H10 to H92
c
W ► E
4m
WF
EF
0
4m
Unit 1 (Pliocene, ca.2.8 Ma)
White carbonate silts with some mm-cm clay levels.
Dark grey to yellow cm thickness laminated clay.
Unit 2 (Pliocene, ca. 2.8 Ma)
Dark grey laminated clay.
Carbonate silts with some mm-cm clay levels.
Red mm-cm grain size gravel interbedded with red coarse sand.
Unit 3 (Middle Pleistocene, ca. 0.9 Ma)
Light yellow carbonate silts interbedded with white lacustrine micrite beds.
Recent deposits
Top soil.
Fluvial terrace.

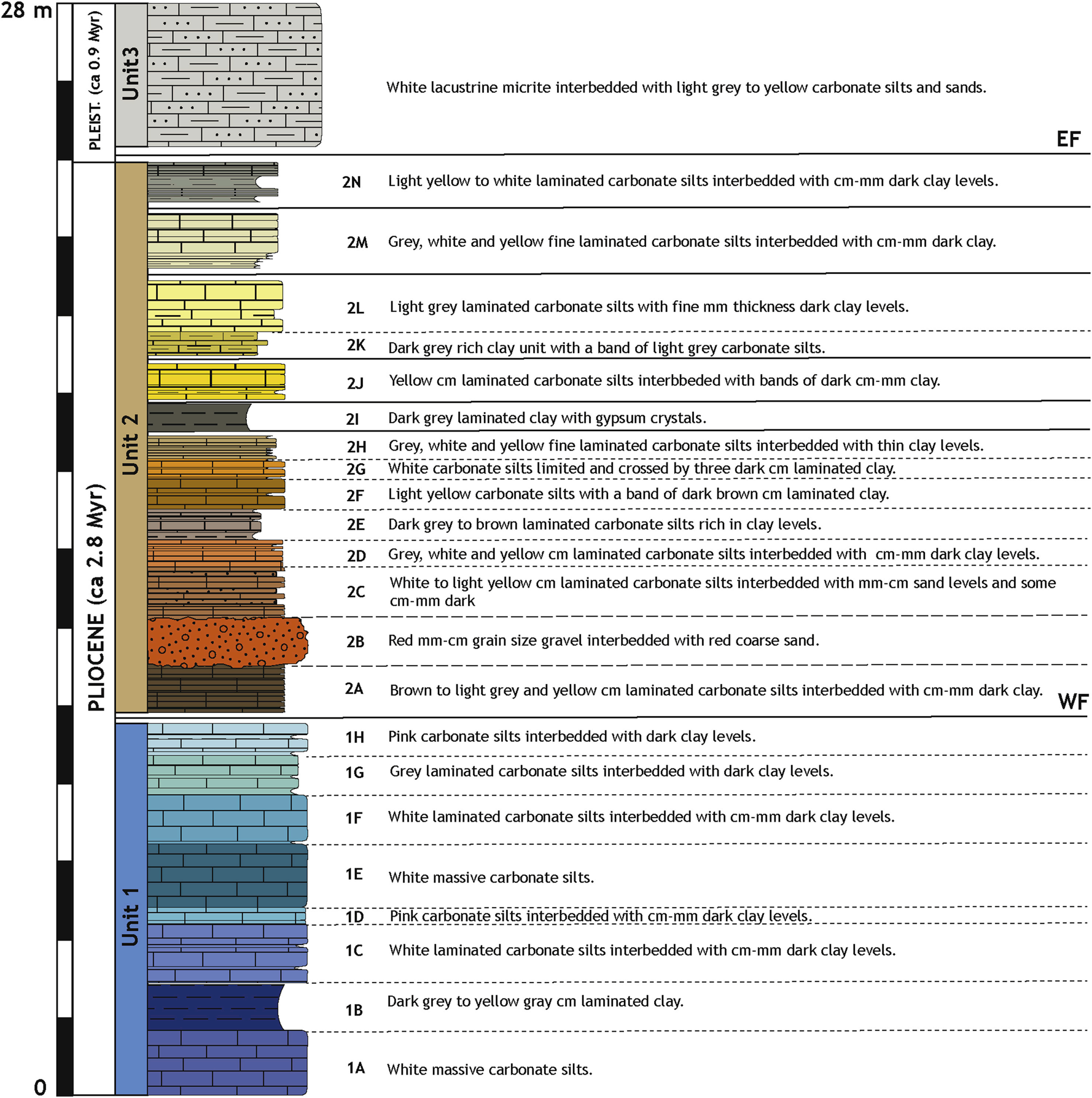
28 m
0
PLEIST. (ca 0.9 Myr)
PLIOCENE (ca 2.8 Myr)
Unit3
Unit 2
Unit 1
White lacustrine micrite interbedded with light grey to yellow carbonate silts and sands.
EF
2N Light yellow to white laminated carbonate silts interbedded with cm-mm dark clay levels.
2M Grey, white and yellow fine laminated carbonate silts interbedded with cm-mm dark clay.
2L Light grey laminated carbonate silts with fine mm thickness dark clay levels.
2K Dark grey rich clay unit with a band of light grey carbonate silts.
2J Yellow cm laminated carbonate silts interbbeded with bands of dark cm-mm clay.
2I Dark grey laminated clay with gypsum crystals.
2H Grey, white and yellow fine laminated carbonate silts interbedded with thin clay levels.
2G White carbonate silts limited and crossed by three dark cm laminated clay.
2F Light yellow carbonate silts with a band of dark brown cm laminated clay.
2E Dark grey to brown laminated carbonate silts rich in clay levels.
2D Grey, white and yellow cm laminated carbonate silts interbedded with cm-mm dark clay levels.
2C White to light yellow cm laminated carbonate silts interbedded with mm-cm sand levels and some cm-mm dark
2B Red mm-cm grain size gravel interbedded with red coarse sand.
2A Brown to light grey and yellow cm laminated carbonate silts interbedded with cm-mm dark clay.
WF
1H Pink carbonate silts interbedded with dark clay levels.
1G Grey laminated carbonate silts interbedded with dark clay levels.
1F White laminated carbonate silts interbedded with cm-mm dark clay levels.
1E White massive carbonate silts.
1D Pink carbonate silts interbedded with cm-mm dark clay levels.
1C White laminated carbonate silts interbedded with cm-mm dark clay levels.
1B Dark grey to yellow gray cm laminated clay.
1A White massive carbonate silts.

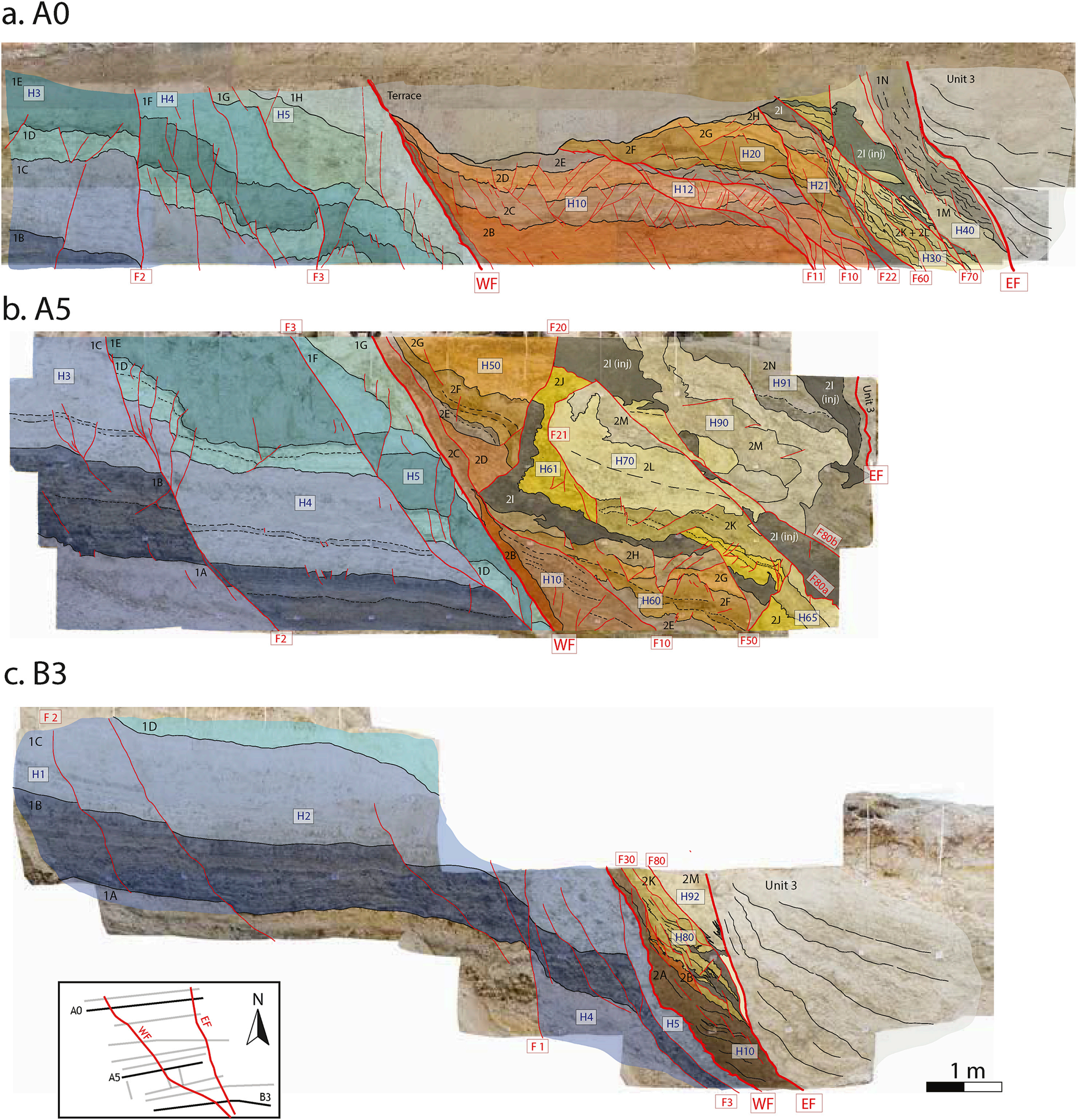
a. A0
1E
H3
1F
H4
1G
1H
H5
1D
1C
1B
Terrace
2D
2E
2F
2G
2H
2I
2C
2B
H10
H12
H20
H21
1N
Unit 3
2I (inj)
1M
2K + 2L
H40
H30
F2
F3
WF
F11
F10
F22
F60
F70
EF
b. A5
F3
F20
1C
1E
1D
1G
1F
2G
2F
2E
2C
2D
H3
H50
2I (inj)
2J
2N
H91
2I
(inj)
Unit 3
2M
H90
F21
H70
2L
H61
1B
H5
H4
2I
2K
2I (inj)
F80b
1A
2B
1D
2H
H10
H60
2G
2F
F80a
2J
H65
2E
F2
WF
F10
F50
EF
c. B3
F 2
1D
1C
H1
1B
H2
1A
F30
F80
2K
2M
H92
Unit 3
H80
2A
2B
H4
H5
H10
F 1
F3
WF
EF
1 m
N
A0
A5
B3

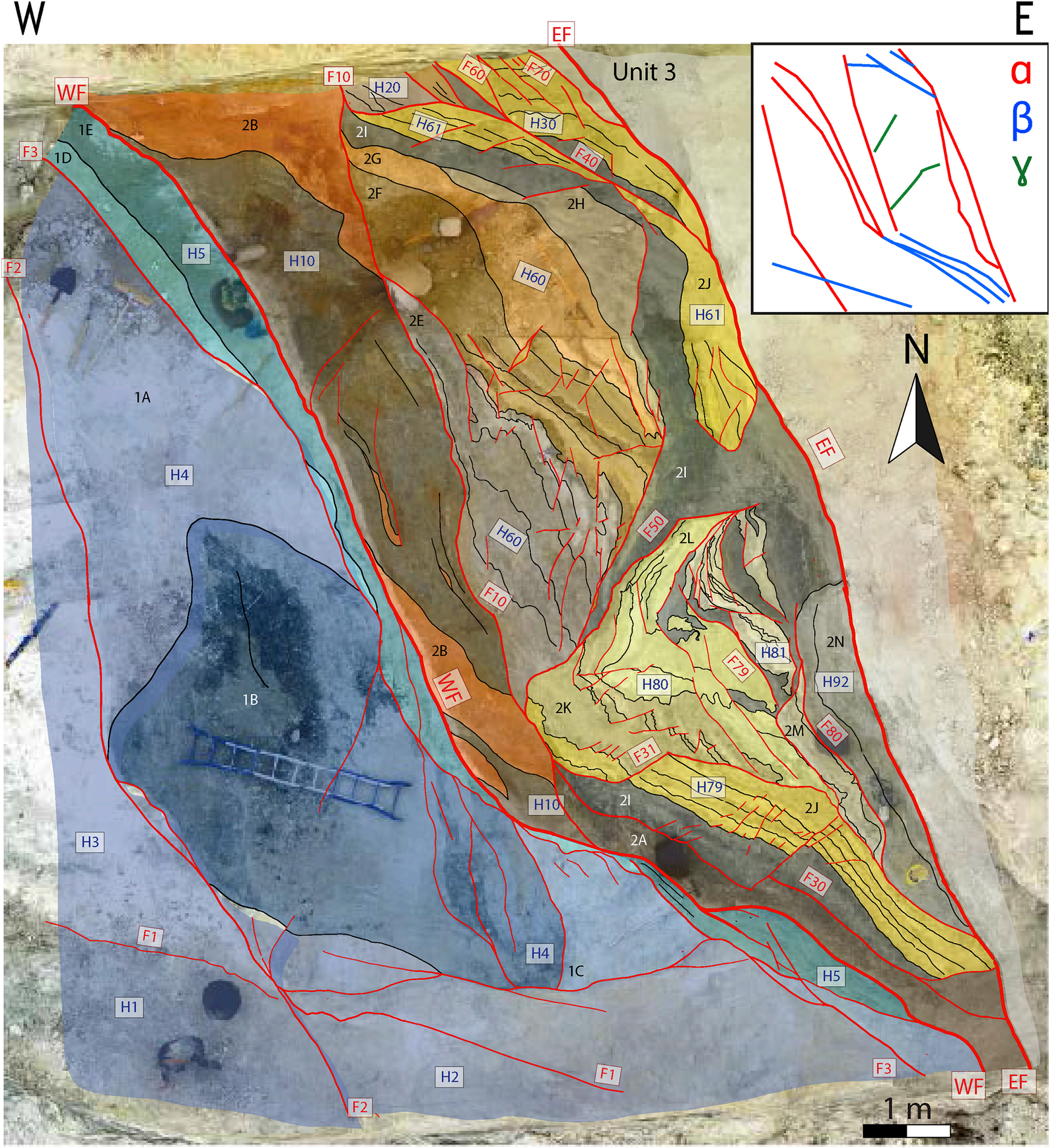
W
E
EF
Unit 3
WF
F10
H20
F60
F70
1E
2B
H61
H30
F3
1D
2I
2G
F40
2F
2H
H5
H10
H60
2J
F2
H61
2E
1A
N
EF
H4
2I
F50
H60
2L
F10
2N
H81
2B
F79
H92
1B
H80
WF
2K
F80
2M
F31
H79
H10
2I
2J
H3
2A
F30
F1
H4
1C
H5
H1
H2
F1
F3
WF
EF
F2
1 m
α
β
γ

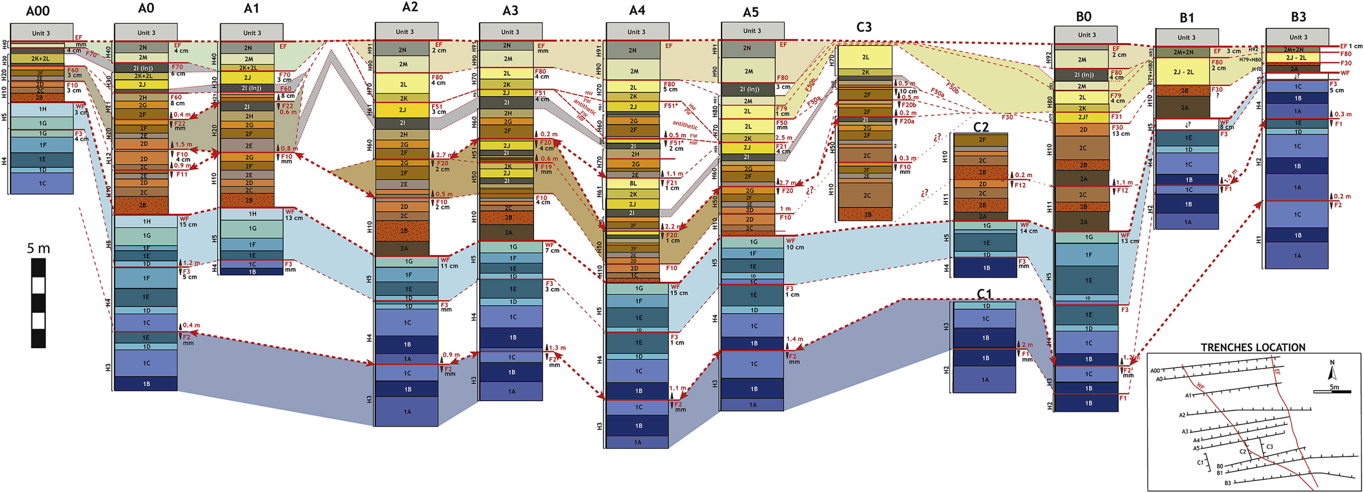

SYMBOLS

- Measurable throw
- Fault throw (1 m)
- Fault name (Fx)
- Máximum fault gouge thickness (x)
- Correlated throw between walls
- Main faults
- Faults
- Antithetic fault
- Subunit 7a correlations
- Unclear correlation
- Hx Rock bodies (horses)

Unit 1

1H	Pink carbonate silts interbedded with dark clay levels.
1G	Grey laminated carbonate silts interbedded with dark clay levels.
1F	White laminated carbonate silts interbedded with some cm-mm thickness dark clay levels.
1E	White massive carbonate silts.
1D	Pink carbonate silts interbedded with some cm-mm thickness dark clay levels.
1C	White laminated carbonate silts interbedded with some cm-mm thickness dark clay levels.
1B	Dark grey to yellow cm thickness laminated clay.
1A	White massive carbonate silts

Unit 2

2N	Light yellow to white laminated carbonate silts interbedded with cm-mm dark clay levels.	2G	Light carbonate silts restricted and crossed by three dark cm thickness laminated clay.
2M	Grey, white and yellow fine laminated carbonate silts interbedded with cm-mm dark clay levels.	2F	Light yellow carbonate silts with a band of dark brown cm thickness laminated clay.
2L	Light grey laminated carbonate silts with some fine mm thickness dark clay levels.	2E	Dark grey to brown laminated carbonate silts rich in clay levels
2K	Dark grey rich clay unit with a band of light grey carbonate silts.	2D	Grey, white and yellow cm thickness laminated carbonate silts interbedded with some cm-mm dark clay levels.
2J	Yellow cm thickness laminated carbonate silts interbbeded with bands of dark cm-mm thickness clay.	2C	Light cm thickness laminated carbonate silts interbedded with mm-cm sand levels and some cm-mm dark clay levels.
2I	Dark grey laminated clay with some gypsum crystals.	2B	Red mm-cm grain size gravel interbedded with red coarse sand.
2H	Grey, white and yellow fine laminated carbonate silts interbedded with some thin clay levels.	2A	Brown to light grey and yellow cm thickness laminated carbonate silts interbedded with cm-mm dark clay.

Unit 3

White lacustrine micrite interbedded with light grey to yellow carbonate silts and sands.

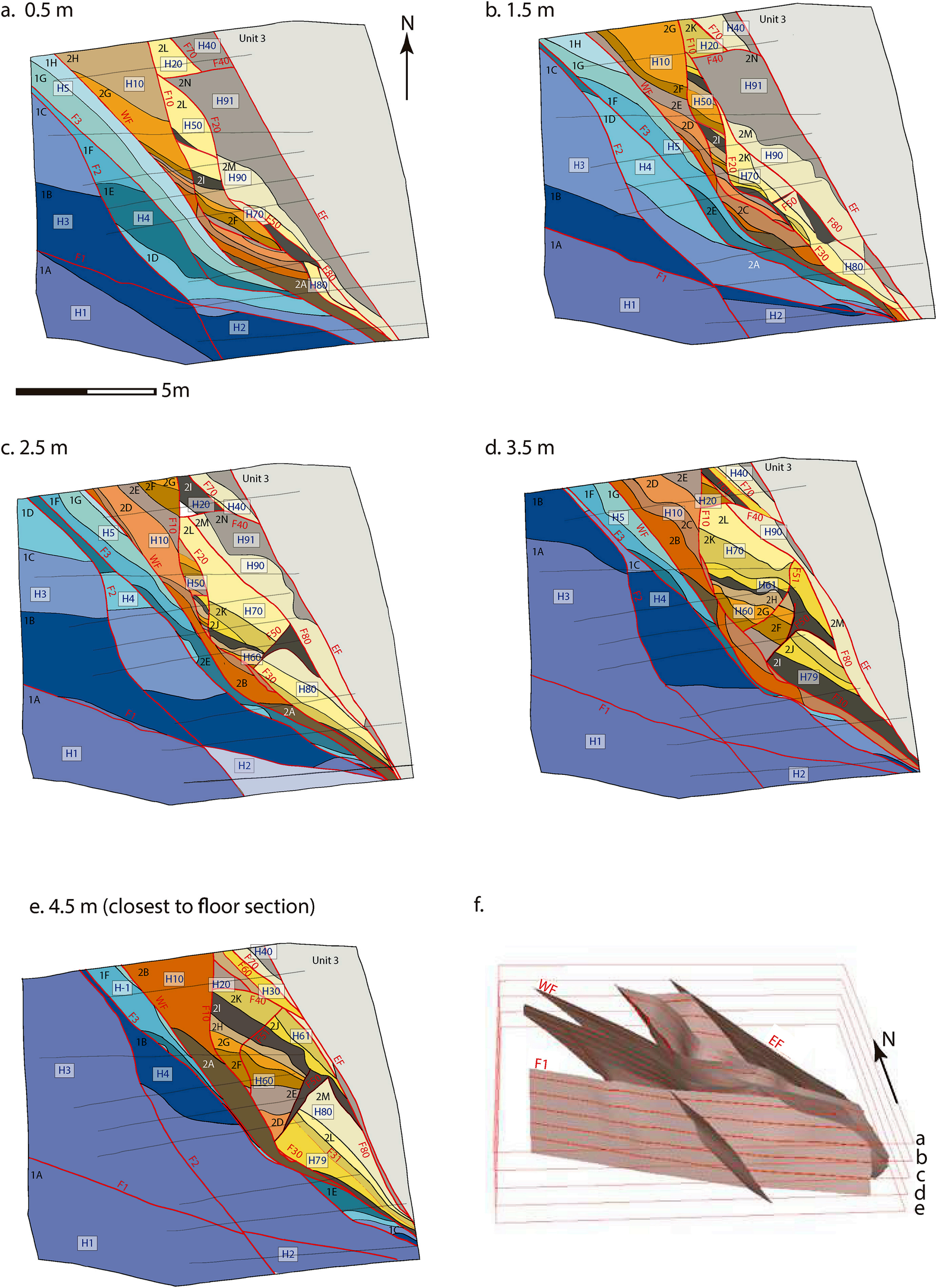

a. 0.5 m
N
Unit 3
1H
2H
2L
H40
H20
F70
F40
1G
H5
H10
2N
H91
1C
2G
F10
2L
WF
F3
H50
F20
1F
2M
F2
2I
H90
1B
1E
H3
H4
2F
H70
F50
EF
F1
1D
F80
1A
2A
H80
H1
H2
5m
b. 1.5 m
Unit 3
2G
2K
F70
H40
1H
F10
H20
F40
1C
1G
H10
2N
WF
2F
H91
1F
2E
H50
1D
F3
2D
2I
2M
F2
H5
H3
H4
2K
H90
F20
H70
1B
F50
EF
2E
2C
F80
1A
F30
2A
H80
F1
H1
H2
c. 2.5 m
Unit 3
2E
2F
2G
2I
F70
1F
1G
H20
H40
1D
2D
F10
2M
2N
F40
H5
H10
2L
H91
1C
F3
WF
F20
H90
H3
H50
F2
H4
2K
H70
1B
2J
F50
F80
EF
2E
H60
F30
2B
H80
1A
2A
F1
H1
H2
d. 3.5 m
Unit 3
H40
2D
2E
F70
1B
1F
1G
H20
H5
H10
F10
2L
F40
WF
2C
H90
F3
2B
2K
1A
H70
1C
F51
H61
H3
F2
H4
2H
H60
2G
2M
2F
F50
2J
F80
EF
2I
H79
F30
F1
H1
H2
e. 4.5 m (closest to floor section)
H40
Unit 3
2B
F70
F60
1F
H10
H-1
H20
H30
2K
F40
WF
F10
2I
2J
F3
2H
H61
1B
2G
EF
H3
H4
2A
2F
H60
F50
2E
2M
H80
2D
2L
F30
H79
F31
F80
F2
1A
1E
F1
1C
H1
H2
f.
WF
EF
N
F1
a
b
c
d
e

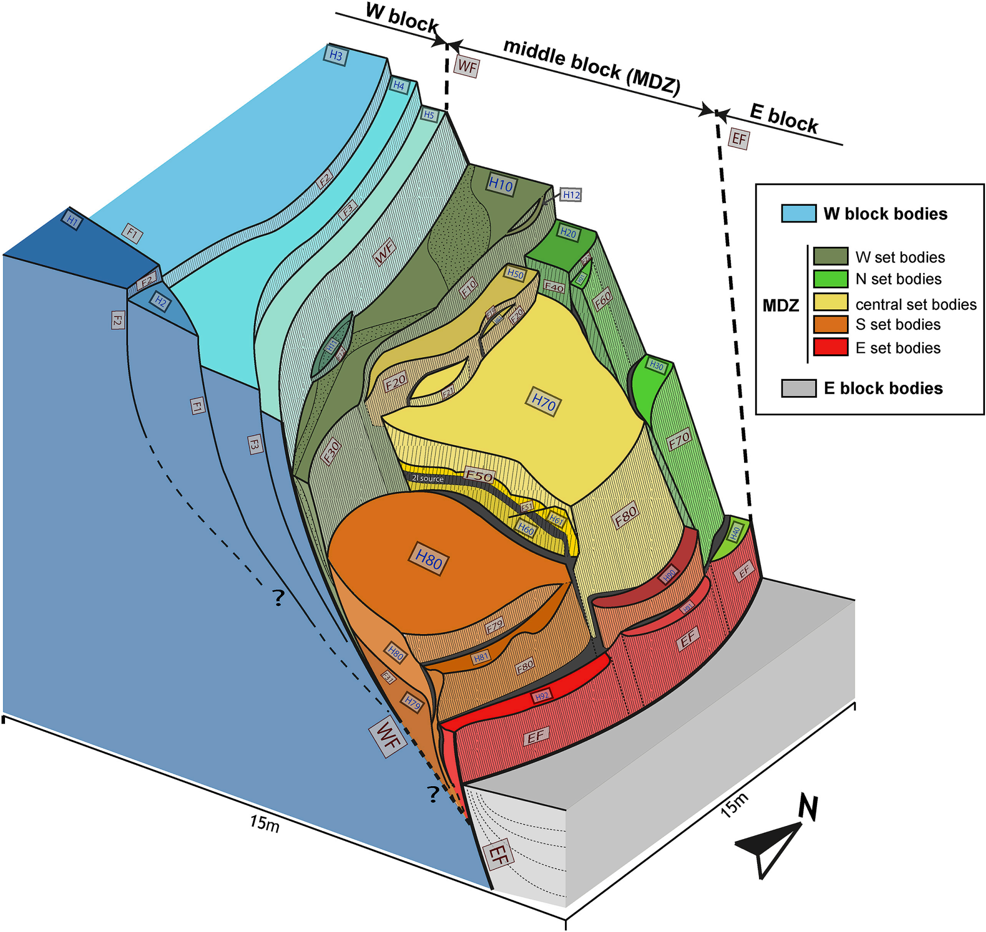

W block
middle block (MDZ)
E block
WF
EF
W block bodies
MDZ
W set bodies
N set bodies
central set bodies
S set bodies
E set bodies
E block bodies
H1
H2
H3
H4
H5
H10
H12
H20
H30
H40
H50
H60
H61
H70
H80
H81
H79
H90
H91
H92
F1
F2
F3
F10
F20
F21
F30
F31
F40
F50
F51
F60
F70
F79
F80
2I source
?
15m
15m
N

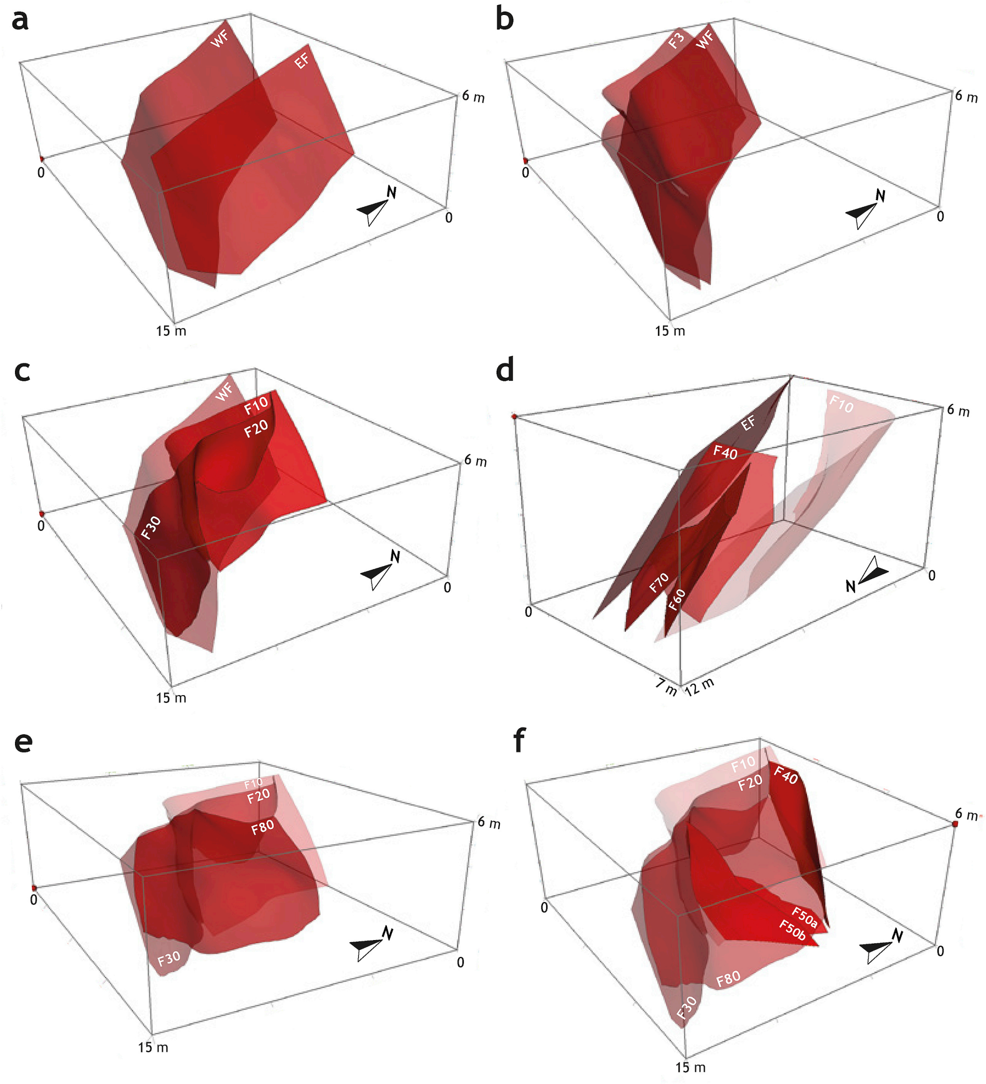
a
WF
EF
6 m
0
0
15 m
N
b
F3
WF
6 m
0
0
15 m
N
c
WF
F10
F20
F30
6 m
0
0
15 m
N
d
EF
F10
F40
F70
F60
6 m
0
0
7 m
12 m
N
e
F10
F20
F80
F30
6 m
0
0
15 m
N
f
F10
F20
F40
F50a
F50b
F80
F30
6 m
0
0
15 m
N

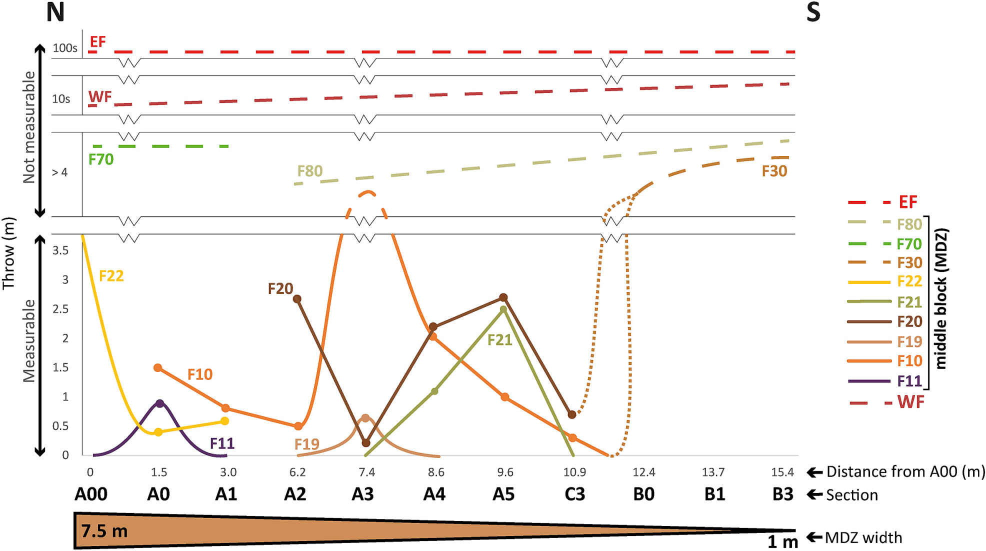

N
S
Throw (m)
Not measurable
Measurable
100s
10s
> 4
EF
WF
F70
F80
F30
F22
F20
F10
F11
F19
F21
3.5
3
2.5
2
1.5
1
0.5
0
0
1.5
3.0
6.2
7.4
8.6
9.6
10.9
12.4
13.7
15.4
← Distance from A00 (m)
A00
A0
A1
A2
A3
A4
A5
C3
B0
B1
B3
← Section
7.5 m
1 m
← MDZ width
middle block (MDZ)

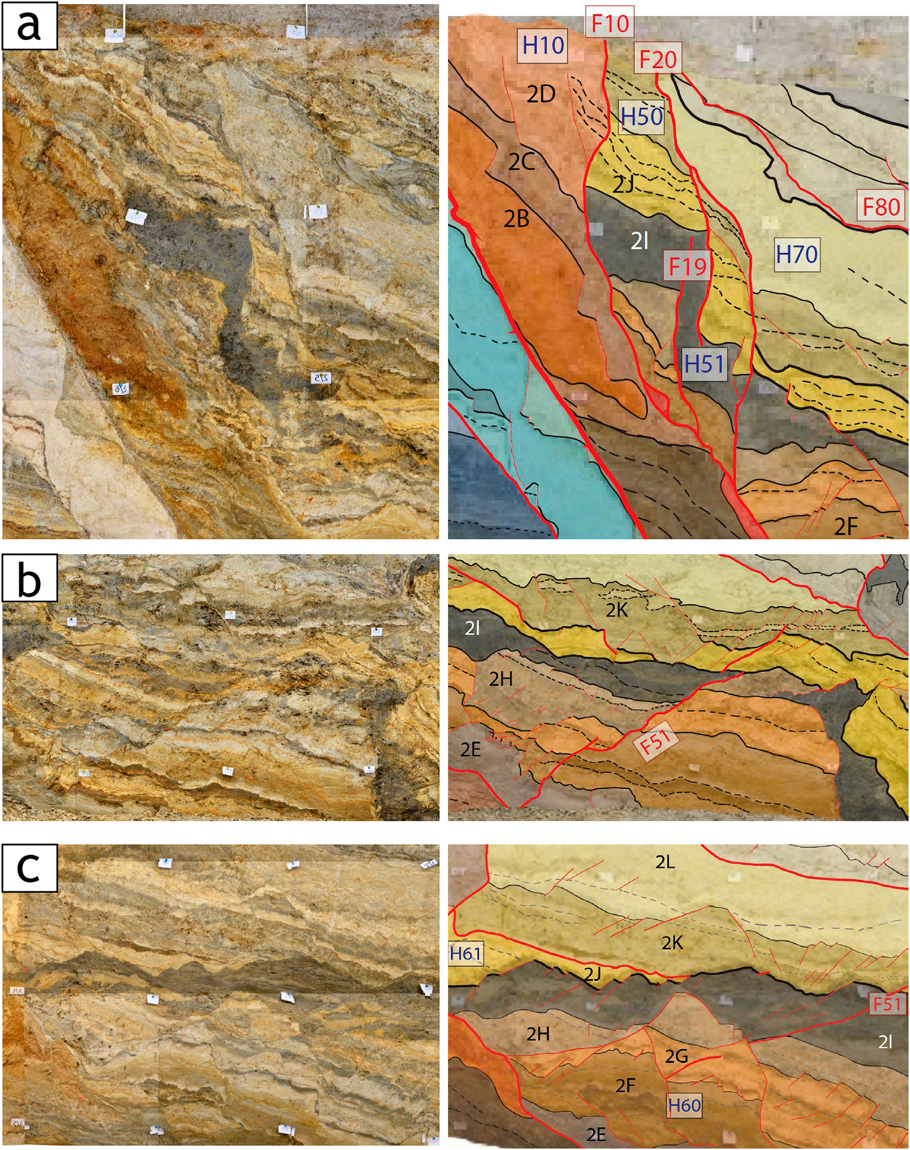
a
F10
H10
F20
2D
H50
2C
2J
F80
2B
2I
F19
H70
H51
2F
b
2K
2I
2H
F51
2E
c
2L
2K
H61
2J
F51
2H
2G
2I
2F
H60
2E

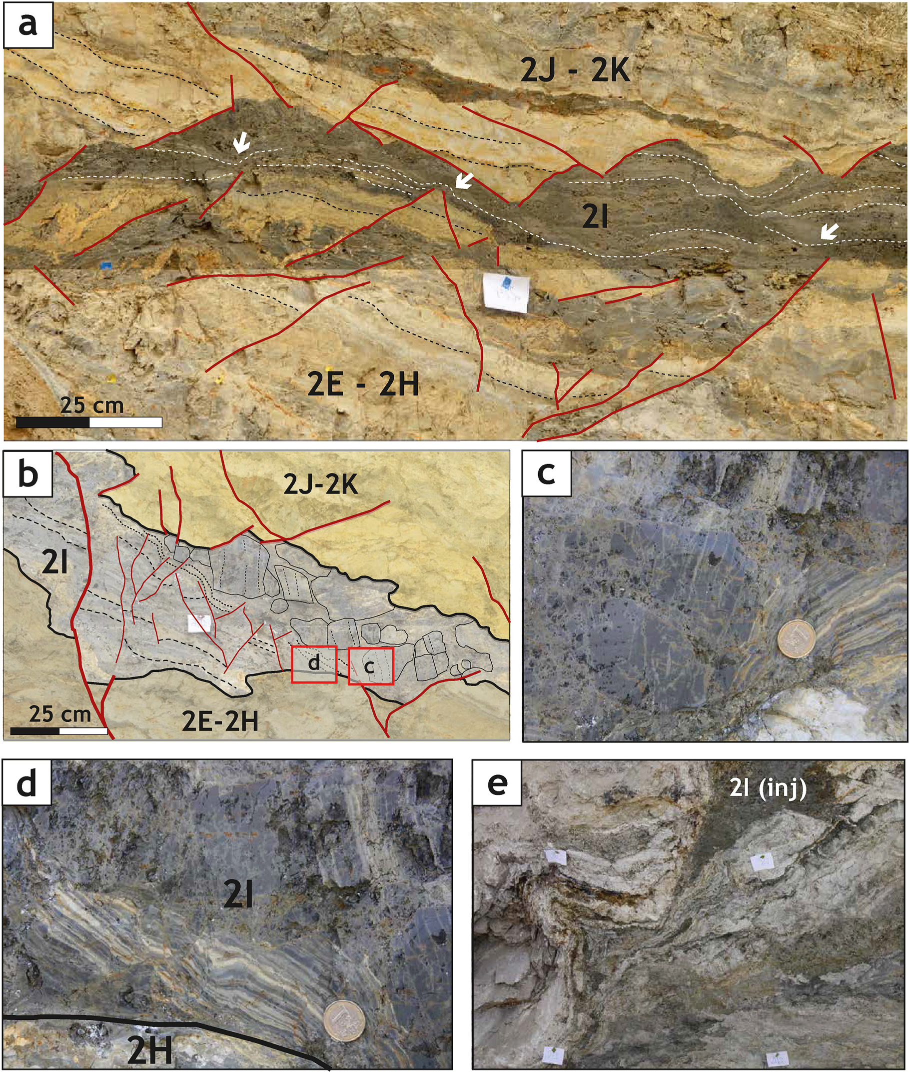
a
2J - 2K
2I
2E - 2H
25 cm
b
2J-2K
2I
d
c
25 cm
2E-2H
c
d
2I
2H
e
2I (inj)

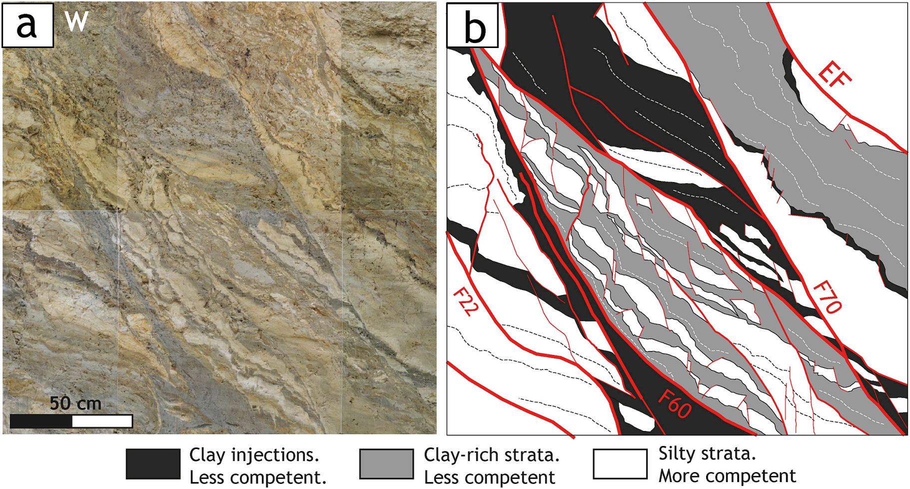

a
W
50 cm
b
EF
F22
F70
F60
Clay injections.
Less competent.
Clay-rich strata.
Less competent
Silty strata.
More competent

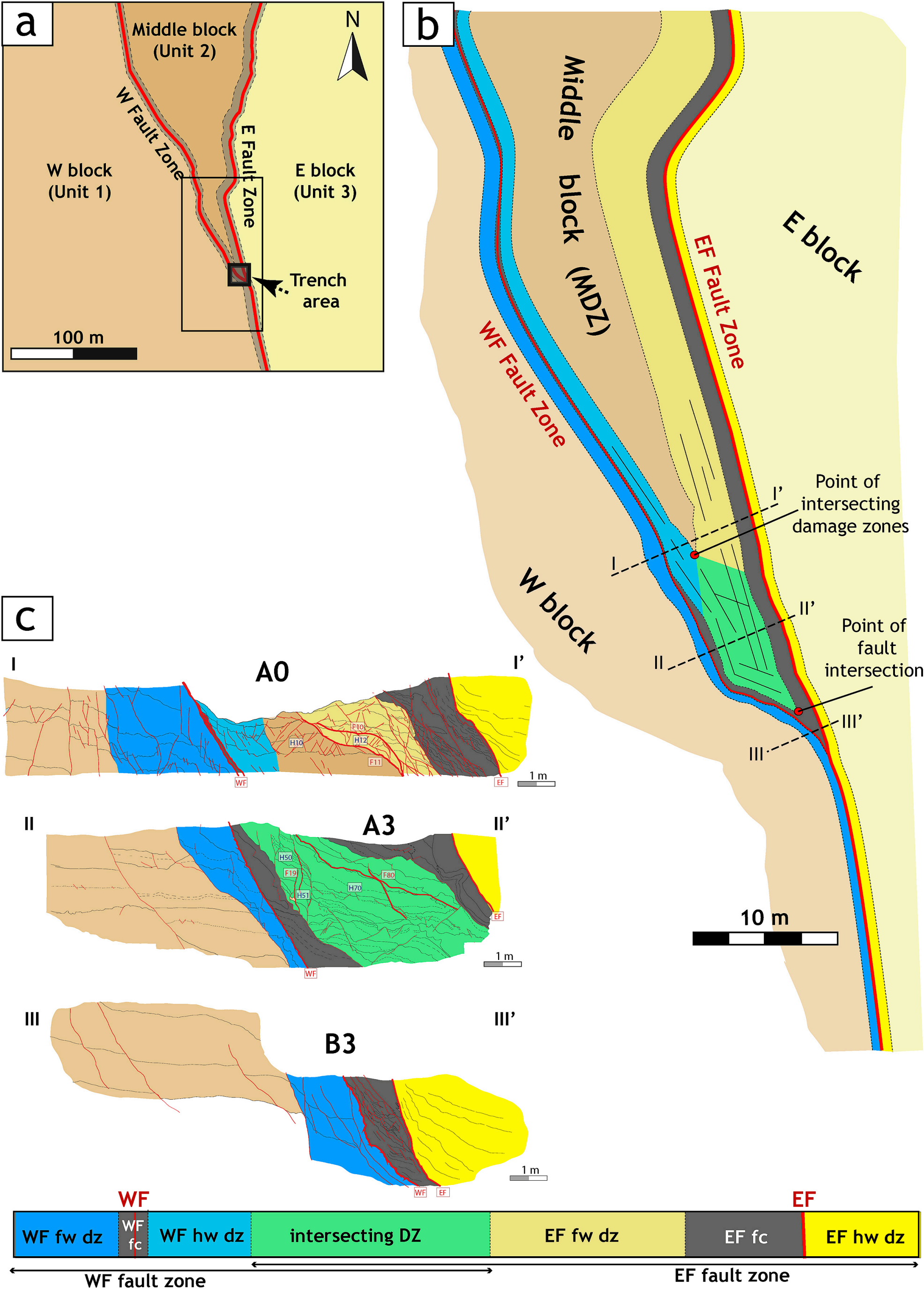

a
Middle block
(Unit 2)
N
W Fault Zone
E Fault Zone
W block
(Unit 1)
E block
(Unit 3)
Trench
area
100 m
b
Middle
block
(MDZ)
E block
EF Fault Zone
WF Fault Zone
Point of
intersecting
damage zones
I
I'
W block
II
II'
Point of
fault
intersection
III
III'
10 m
c
I
A0
I'
H10
F10
H12
F11
WF
EF
1 m
II
A3
II'
H50
F19
H51
H70
F80
EF
WF
1 m
III
B3
III'
1 m
WF
EF
WF
EF
WF fw dz
WF fc
WF hw dz
intersecting DZ
EF fw dz
EF fc
EF hw dz
WF fault zone
EF fault zone

- A 3D trench study reveals the complexity of a normal fault zone in soft sediments.
- Highly variable rock bodies, faults, smears and clay injections form the fault zone.
- Variable fault geometries and throws cause a variable distribution of deformation.
- Mechanical stratigraphy has a key role in the variability and style of deformation.
- As main strands approach, fault throw, deformation and fault zone maturity increase.
- This 4D picture of fault deformation is key for modelling fluid flow in faulted reservoirs.